The effect of faceting on olivine wetting properties

Yongsheng Huang[1], Takayuki Nakatani[1], Sando Sawa[1], Michihiko Nakamura[1], and Catherine Mccammon[2]

[1]Tohoku University
[2]University of Bayreuth

November 22, 2022

Abstract

Grain-scale pore geometry primarily controls the fluid distribution in rocks, affecting material transport and geophysical response. The dihedral angle (Θ) in the olivine–fluid system is a key parameter determining the pore fluid geometry in mantle wedges. Both curved and faceted olivine–fluid interfaces define Θ in the system, generating the faceted–faceted (FF), faceted–curved (FC), and curved–curved (CC) angles. However, the effect of faceting on Θ under various pressure and temperature (P–T) conditions and fluid compositions have not been constrained, and its mineralogical understanding is unresolved. This study evaluates the facet-bearing Θ and their proportions in olivine–multicomponent aqueous fluid systems. Our results show that 1/3 of olivine–fluid Θ are facet-bearing angles irrelative to the P–T conditions and fluid compositions. Faceting produces larger dihedral angles than the CC angles. The grain boundary plane (GBP) distribution reveals that the GBPs of faceted interfaces at triple junctions were subjected to low Miller Index faces ((100), (010), and (101)). Moreover, calculating the FF angles from two adjacent low Miller index planes highly reproduces measured angle values based on the olivine crystal habit. Therefore, our study suggests that the FF angle is strongly affected by olivine crystallography. The presence of faceting increases Θ and critical fluid fraction (Φc) for percolation, thus decreases the permeability. In the mantle wedge, where olivine crystallographic preferred orientation (CPO) is expected, increasing the FF angle proportion with associated changes in fluid pore morphology will lead to the permeability anisotropy and consequent geophysical anomalies.

The effect of faceting on olivine wetting properties

Yongsheng Huang[1*, a], Takayuki Nakatani[1, b], Sando Sawa[1, c], Michihiko Nakamura[1], Catherine McCammon[2]

1. Department of Earth Science, Graduate School of Science, Tohoku University, Aramaki–Aza–Aoba, Aoba–Ku, Sendai, Miyagi 980–8578, Japan

2. Bayerisches Geoinstitut, University of Bayreuth, 95440 Bayreuth, Germany

a. Current address: Guangzhou Institute of Geochemistry, Chinese Academy of Sciences, 511 Kehua Street, Wushan, Tianhe, Guangzhou 510640, China.

b. Current address: Geological Survey of Japan, AIST Central 7, Higashi 1–1–1, Tsukuba, Ibaraki 305–8567, Japan.

c. Current address: Division of Advanced Mechanical Systems Engineering, Institute of Engineering, Tokyo University of Agriculture and Technology, Nakamachi 2-24-16, Koganei, Tokyo, 184-0012, Japan.

* Corresponding author. Email: huangyongsheng@gig.ac.cn

Key points

1. Faceting produces larger dihedral angles than those with curved interfaces in the olivine–fluid system.
2. Grain boundary planes are frequently composed of low–index planes, and the facet–facet angles are explained by olivine crystallography.
3. The facet proportion is consistent with electrical conductivity data; faceting effects could be magnified under a sheared-wedge mantle.

Abstract

Grain-scale pore geometry primarily controls the fluid distribution in rocks, affecting material transport and geophysical response. The dihedral angle (θ) in the olivine–fluid system is a key parameter determining the pore fluid geometry in mantle wedges. Both curved and faceted olivine–fluid interfaces define θ in the system, generating the faceted–faceted (FF), faceted–curved (FC), and curved–curved (CC) angles. However, the effect of faceting on θ under various pressure and temperature (P–T) conditions and fluid compositions have not been constrained, and its mineralogical understanding is unresolved. This study evaluates the facet-bearing θ and their proportions in olivine–multicomponent aqueous fluid systems. Our results show that 1/3 of olivine–fluid θ are facet-bearing angles irrelative to the P–T conditions and fluid compositions. Faceting produces larger dihedral angles than the CC angles. The grain boundary plane (GBP) distribution reveals that the GBPs of faceted interfaces at triple junctions were subjected to low Miller Index faces ((100), (010), and (101)). Moreover, calculating the FF angles from two adjacent low Miller index planes highly reproduces measured angle values based on the olivine crystal habit. Therefore, our study suggests that the FF angle is strongly affected by olivine crystallography. The presence of faceting increases θ and critical fluid fraction (ϕ_c) for percolation, thus decreases the permeability. In the mantle wedge, where olivine crystallographic preferred orientation (CPO) is expected, increasing the FF angle proportion with associated changes in fluid pore morphology will lead to the permeability anisotropy and consequent geophysical anomalies.

Plain Language Summary

Pore geometry controls fluid-bearing rocks' material transport and geophysical properties, affecting elemental cycling and the interpretation of magnetotelluric and seismological observations in subduction zones. The dihedral angle (θ) in the olivine–fluid system is a key parameter determining fluid geometry in a mantle wedge. Both curved and faceted olivine–fluid interfaces appear, but the effect of faceting on θ under various P–T conditions and fluid compositions is poorly constrained. Here, we measured the facet-bearing θ and their proportions in olivine–multicomponent aqueous fluid systems. The results show that 1/3 of olivine–fluid θ are facet-bearing irrelative of the P–T conditions and fluid compositions. The θ values of the facet–bearing angle are comparable to, or larger than, the curved–curved angle. Both grain boundary planes of faceted olivine–fluid interfaces are preferentially subjected to low Miller Index faces; thus, the FF angle is strongly affected by olivine crystallography. The presence of faceting increases θ, the critical fluid fraction (ϕ_c), and decreases the permeability. In the mantle wedge, where olivine crystallographic preferred orientation (CPO) is expected, the presence of an FF angle with associated changes in fluid pore morphology will lead to permeability anisotropy and geophysical anomalies.

Key words: dihedral angle, faceted plane, Miller Index, crystallographic orientation, fluid connectivity, permeability anisotropy.

1. Introduction

Pore geometry significantly controls the distribution of geological fluid (i.e., aqueous fluid and silicate melt) in a deep mantle wedge, thereby affecting element cycling and geophysical response in subduction zones (Watson & Brenan, 1987; Hermann et al., 2006; Iwamori, 1998; van Keken et al., 2011; Pommier & Evans, 2017; Worzewski et al., 2011; Zheng et al., 2016). Although channelized fluid flow has often been inferred from the field studies (Angiboust et al., 2014), the pervasive grain-scale fluid flow may be the most plausible fluid migration regime at high pressure (P) and high temperature (T) conditions where dissolution-precipitation intensively operates and interfacial energy minimization ("textural equilibrium") is quickly attained. Moreover, the pervasive nature may be suitable for explaining the resistivity anomalies observed at a magnetotelluric (MT) grid-scale (commonly >10 km), because it would be required for the channelized flows to be distributed continuously and nearly isotropically over this length scale. In an olivine-dominant mantle rock, the olivine–fluid dihedral angle (θ) is the primary parameter controlling the grain-scale fluid connectivity (Huang et al., 2019, 2020; Mibe et al., 1999; Toramaru & Fujii, 1986). Therefore, a precise constraint on θ in the olivine–fluid system is important for a complete understanding of the fluid distribution and migration in subduction zones.

The dihedral angle is a consequence of the fluid–mineral interaction, which changes the fluid pore geometry through dissolution and precipitation processes to minimize the interfacial energy in the system. It is defined as the ratio of the grain boundary energy (γ_{ss}) to the solid–fluid interfacial energy (γ_{sf}) (von Bargen & Waff, 1986; Watson & Brenan, 1987) as follows:

$$2\cos(\theta/2) = \gamma_{ss}/\gamma_{sf} \quad (1).$$

In an isotropic system, where solid–fluid interfaces are smoothly curved with a constant mean curvature, the geometry of the intergranular fluid is solely determined by the dihedral angle. Fluids can wet the grain edges well and migrate along with interconnected tubular networks at $\theta < 60°$ irrespective of the fluid fraction (ϕ). In contrast, the fluid is distributed as isolated pockets along the grain edges, corners, and boundaries at $\theta > 60°$ when ϕ is lower than the critical value (ϕ_c) (Watson & Brenan, 1987; Holness, 1992, 1993), which is dependent on θ (von Bargen & Waff, 1986). However, the fluid distribution in the realistic rocks can deviate from the ideal distribution (Laporte & Watson, 1995; Waff & Faul, 1992). In fact, Huang et al. (2021) measured the electrical conductivity of the texturally equilibrated forsterite–saline fluid aggregate at 800°C and 1 GPa showing that the conductivity is significantly smaller than that expected from the interconnected tube model especially at low ϕ. The synchrotron X–ray microtomography (CT) of the post-run products revealed that the fluid pores gradually get interconnected with each other, increasing ϕ above ~1.0 % even though θ defined by the curved–curved interface is smaller than 60° under the experimental conditions (Huang et al., 2019).

In a realistic mineral–fluid system with interfacial energy anisotropy, facet planes, crystallographically controlled planar solid–liquid interfaces, are often present along with the curved interface (Watson & Lupulescu, 1993; Price et al., 2006; Wark & Watson, 2000; Watson, 1999). The coexistence of both curved and faceted interfaces generates three types of θ: curved–curved (CC), faceted–curved (FC), and faceted–faceted (FF) θ (Yoshino et al., 2006). Pores surrounded by facet planes are difficult to connect unless ϕ increase above the critical value which depends on θ defined by the faceted interfaces (Price et al., 2006). Therefore, the facet plane may affect the fluid connectivity depending on its θ values, which helps to explain the results of

electrical conductivity measurements in Huang et al. (2021). Price et al. (2006) reported that facet bearing angles are larger than those of the curved–curved interfaces in the quartz–fluid and tremolite–fluid systems. If this is the case, facet-bearing pores may require the relatively high ϕ for the fluid interconnection. Although many studies have been conducted to investigate the P–T, fluid composition, and mineral assemblage dependence of θ in the olivine–fluid system (Watson & Brenan, 1987; Huang et al., 2019, 2020; Mibe et al., 1998, 1999; Yoshino et al., 2006), the effect of the angle–type variation on θ is poorly understood. Yoshino et al. (2006) systematically investigated the effect of faceting on pore geometry in texturally equilibrated rocks and discussed its implications for permeability in several representative systems, including the San Carlos olivine–MORB melt. However, olivine (forsterite)–aqueous fluid systems have not yet been studied. Huang et al. (2019, 2020) studied the dihedral angle between olivine and multicomponent aqueous fluids over a wide range of pressures and temperatures, but they primarily focused on the CC θ. Laporte and Provost (2000) theoretically investigated the θ in the system with simplified surface energy anisotropy and reported that the relationship between the mean equilibrium θ and the ratio of the grain boundary to the surface energy is close to the isotropic case. Nevertheless, empirical investigation of the facet-bearing dihedral angles concerning crystallographic orientations remains unresolved for actual mineral–fluid systems.

Investigating the grain boundary plane distribution (GBPD) can provide a mineralogical understanding of angle–types in terms of the FF, FC, and CC angles. Some researchers previously investigated GBPD in the fluid-free olivine polycrystals and found that low Miller Index planes preferentially appears in the grain boundaries (Faul & Fitz Gerald, 1999; Marquardt et al., 2015). If such specific grain boundary planes (GBPs) preferentially appear at the facet-bearing triple junctions in the mineral–fluid system, they may significantly control θ of the facet-bearing angles

and its resultant fluid pore geometry. However, previous studies did not distinguish the grain boundary type in terms of the angle–types (i.e., FF, FC, and CC), and the GBPD has not been examined in the fluid-bearing system.

In this study, we investigated the facet-bearing (i.e., FF and FC) θ in the run products of the olivine–fluid systems previously obtained by piston–cylinder experiments at various pressures (P: 1–3 GPa), temperatures (T: 800–1100 °C), and fluid compositions (pure H_2O, H_2O–NaCl, and H_2O–CO_2 systems) (Huang et al., 2019, 2020). These results were compared with the CC θ to clarify the effect of faceting. Moreover, we examined the crystallographic orientation of the olivine aggregate and identified the GBPD at triple junctions with different angle–types to evaluate the influence of the crystallographic orientations on θ. Based on the results, we discussed the origin of faceting and its effect on θ and inferred the consequences of faceting on the fluid connectivity, fluid distribution, and permeability anisotropy in the olivine–fluid system under static and sheared mantle conditions.

2. Methods

2.1. Samples

We analyzed the run products of the olivine–fluid systems previously obtained by Huang et al. (2020, 2019). To constrain the P–T and fluid composition dependency of the facet-bearing θ, we selected 19 samples that cover a wide range of experimental P–T conditions (1–3 GPa and 800–1100 °C) and fluid compositions (H_2O, H_2O–CO_2 with $X_{(CO2)} = CO_2/(H_2O+CO_2) = 0.5$ in molar ratio), and H_2O–NaCl with 5.0 and 27.5 wt.%NaCl). The run products containing magnesite and orthopyroxene due to olivine carbonation (Huang et al., 2020) were not included in the present study to avoid the effect of mineral species other than olivine.

Herein, we summarize the experimental procedures employed in a previous study (Huang et al., 2020, 2019) to synthesize the samples. High P–T experiments were conducted at Bayerisches Geoinstitut, University of Bayreuth, using end-loaded piston–cylinder apparatus. Piston diameters of 3/4 inch and 1/2 inches were used for the experiments at pressures of 1–2 GPa and 3 GPa, respectively, along with a standard Talc–Pyrex assembly (Keppler et al., 2003). The starting material was San Carlos olivine powder ($Fo_{91}Fa_9$) with grain sizes of 38–53 μm. Deionized and distilled water were used as the pure H_2O sources. Pure oxalic acid dihydrate ($C_2H_2O_4 \cdot 2H_2O$) was used as the CO_2 source. To obtain the NaCl solution, we dissolved reagent-grade NaCl (99.99% NaCl) in deionized and distilled water at room temperature (~25°C) and atmospheric pressure. Water and hydrous oxalic acid were mixed to obtain the target $X_{(CO2)}$. The olivine powder, combined with around 3.0 wt% fluid, was loaded into the end-welded noble metal capsule that was sealed by arc welding. The Au capsules (2.2 mm outer diameter) and $Au_{80}Pd_{20}$ alloy capsules (2.0 mm outer diameter) were used for experiments at 800–1000 °C and 1100°C, respectively. The detailed procedures employed for the high P–T experiments were provided by Huang et al. (2019, 2020). The run duration ranged from 72 h to 211 h, depending on the target temperature. The experimental conditions and results are summarized in Table 1. In our experiments, CO_2 was assumed to be the predominant C species based on previous studies (Allen & C., 1972; Huang et al., 2020; Médard et al., 2008).

The post-run capsules were cut using a diamond wire saw to expose the run products. The run products were then impregnated with an epoxy resin under a vacuum. We first polished these products using the sandpaper and diamond past with particle sizes down to 1.0 μm and then a 0.06 μm colloidal silica suspension. For electron backscattered diffraction (EBSD) analysis, the

178 samples were polished with colloidal silica suspension for more than 10 h using an automatic
179 vibratory polishing machine (VibroMet, Buehler Ltd.).

180 **2.2. Scanning Electron Microscope (SEM)**

181 We observed polished cross-sections of the run charges using a field-emission type
182 scanning electron microscope (FE–SEM; JSM–7100F, JEOL Ltd.) with an accelerating voltage of
183 15 keV. The mineral phases and micro-texture of samples were observed. We took FF and FC type
184 triple junctions for quantitative analysis. More than 300 backscattered electron (BSE) or secondary
185 electron (SE) images of 1280 × 960 pixels were obtained for each run product with high
186 magnifications and resolution, depending on the pore size.

187 **2.3. Dihedral angle measurement**

188 The apparent FF and FC θ were measured at the triple junctions on the SEM images using
189 the Image–J software. We followed the method used for the CC angle measurements in Huang et
190 al. (2019, 2020). The median of measured angles was regarded as true θ (Jurewicz & Jurewicz,
191 1986). Generally, the median of measured angles is close to the true θ value to the greatest extent
192 when a sufficient number of angles are measured by using high magnification and high-resolution
193 SEM images. However, a deviation between the median and true angle could have occurred when
194 the sample suffered from severe plucking during cutting and polishing, which locally reduced the
195 randomness of the apparent angle distribution. Although Cmíral et al. (1998) demonstrated that θ
196 values obtained with transmission electron microscopy (TEM) was smaller than those measured
197 from low magnification SEM images, our FE–SEM images were taken at a high magnification (up
198 to 150,000) and provided clear images comparable with those by TEM. In this study, more than
199 100 angles were measured on the acquired SE images for each angle–type for each sample. The

statistical error of the median value was estimated to be less than 1.5°, as discussed by Huang et al. (2020). The details of θ selection and measurement are given in Huang et al. (2019).

2.4. Electron Backscattered Diffraction (EBSD)

To identify the crystallographic orientation of the olivine aggregate and its consequences on θ, we mapped 10 representative samples by using FE–SEM equipped with an electron backscatter diffraction (EBSD; HKL Channel5, Oxford Instruments plc.) at Tohoku University. Analyses were conducted at an accelerating voltage of 15.0 kV. Two types of EBSD data were collected for each sample. One was obtained with lower magnification (×200–500) to investigate the crystallographic preferred orientation (CPO) of the entire sample, and the other with higher magnification (×5,000–15,000) to identify the crystallographic orientation near the fluid pool. The EBSD data were then processed using the MTEX MATLAB toolbox. Grain boundaries were detected using a threshold misorientation angle of 10°. Grains smaller than two or three pixels were removed, depending on the step size (250 nm). The grain-size distribution and CPO were constructed from one point per data point.

Table 1. Experimental conditions and results

Run no.	P (GPa)	T (°C)	Duration (h)	Fluid phase	Salinity (wt%)	$X(CO_2)$	Statistic angle number for faceting ratio	Faceting proportion (%)	EBSD	GBPD	Angle Type	Number of angle measured	Median (Degree)	I&D group
1	1	800	192	H_2O	0	-	187	32.6	-	-	FF	112	70.8	I
											FC	174	70.4	
											CC[a]	200	71.2	
											All	486	71.0	
2	1	800	192	H_2O-NaCl	5	-	218	31.9	-	-	FF	137	68.4	D
											FC	176	63.1	
											CC[a]	222	58.5	
											All	535	62.0	
3	1	800	192	H_2O-NaCl	27.5	-	309	32.9	-	-	FF	120	66.3	D
											FC	126	62.3	
											CC[a]	207	58.3	
											All	453	60.6	
4	1	1000	120	H_2O	0	-	509	30.4	√	√	FF	134	63.6	I
											FC	143	64.2	
											CC[a]	210	64.1	
											All	487	63.8	
5	1	1000	120	H_2O-CO_2	0	0.5	383	32.1	√	√	FF	148	79.2	I
											FC	171	78.4	
											CC[b]	213	78.2	
											All	532	78.5	
6	1	1000	120	H_2O-NaCl	27.5	-	302	32.0	√	√	FF	115	62.0	D
											FC	174	59.7	
											CC[a]	208	56.1	
											All	497	57.8	
7	2	800	212	H_2O	0	-	205	31.8	√	-	FF	136	68.7	I
											FC	178	68.8	
											CC[a]	212	69.9	
											All	526	69.1	
8	2	800	192	H_2O-NaCl	5	-	201	33.3	√	√	FF	118	64.3	D
											FC	172	57.9	
											CC[a]	247	53.6	
											All	537	56.4	
9	2	800	210	H_2O-NaCl	27.5	-	269	31.3	√	√	FF	107	66.5	D
											FC	178	59.0	
											CC[a]	210	56.4	
											All	495	59.0	
10	2	1000	120	H_2O	0	-	582	33.5	√	√	FF	102	58.4	I
											FC	249	57.5	
											CC[a]	213	58.0	
											All	564	57.8	
11	2	1000	133	H_2O-NaCl	5	-	314	32.8	√	√	FF	101	50.7	D
											FC	188	46.5	
											CC[a]	201	43.4	
											All	490	45.0	
12	2	1000	120	H_2O-NaCl	27.5	-	136	33.8	√	√	FF	120	57.0	D
											FC	159	55.6	
											CC[a]	304	51.7	
											All	583	53.7	
13	2	1100	72	H_2O	0	-	284	34.2	-	-	FF	134	59.1	D
											FC	153	56.9	
											CC[a]	210	53.8	
											All	497	55.9	
14	2	1100	72	H_2O-NaCl	27.5	-	201	30.0	-	-	FF	104	58.3	D
											FC	224	52.6	
											CC[a]	202	47.1	
											All	530	50.2	
15	3	800	211	H_2O	0	-	100	35.8	-	-	FF	123	64.9	I
											FC	135	65.0	
											CC[a]	200	66.2	
											All	458	66.0	
16	3	800	192	H_2O-NaCl	5	-	166	33.6	-	-	FF	107	55.0	D
											FC	132	53.2	
											CC[a]	242	50.2	
											All	481	52.4	
17	3	800	211	H_2O-NaCl	27.5	-	157	36.9	-	-	FF	103	64.0	D
											FC	164	60.2	
											CC[a]	200	56.4	
											All	467	60.0	
18	3	1000	120	H_2O	0	-	344	28.3	-	-	FF	110	60.6	D
											FC	199	54.7	
											CC[a]	205	49.2	
											All	514	53.7	
19	3	1000	120	H_2O-NaCl	27.5	-	158	30.0	√	√	FF	102	61.4	D
											FC	147	55.5	
											CC[a]	220	47.4	
											All	469	51.6	

Note: The fluid fraction in each experiment was ~3.0 wt.%. The true θ value for each system was a median value ± 1.5°. The analytical error for the faceting proportion was 0.5%. **a** the CC is cited from Huang et al. (2019); **b** the CC is cited from Huang et al. (2020). The run products that were employed for the electron backscattered diffraction (EBSD) and grain boundary plane distribution (GBPD) are marked in the table. $X_{(CO2)} = CO_2/(H_2O+CO_2)$ in mole.

Abbreviations: ol = olivine, FF = faceted–faceted angle, FC = faceted–curved angle, CC = curved–curved angle, All = all measured angles, I = angle–type independent group, D = angle–type dependent group.

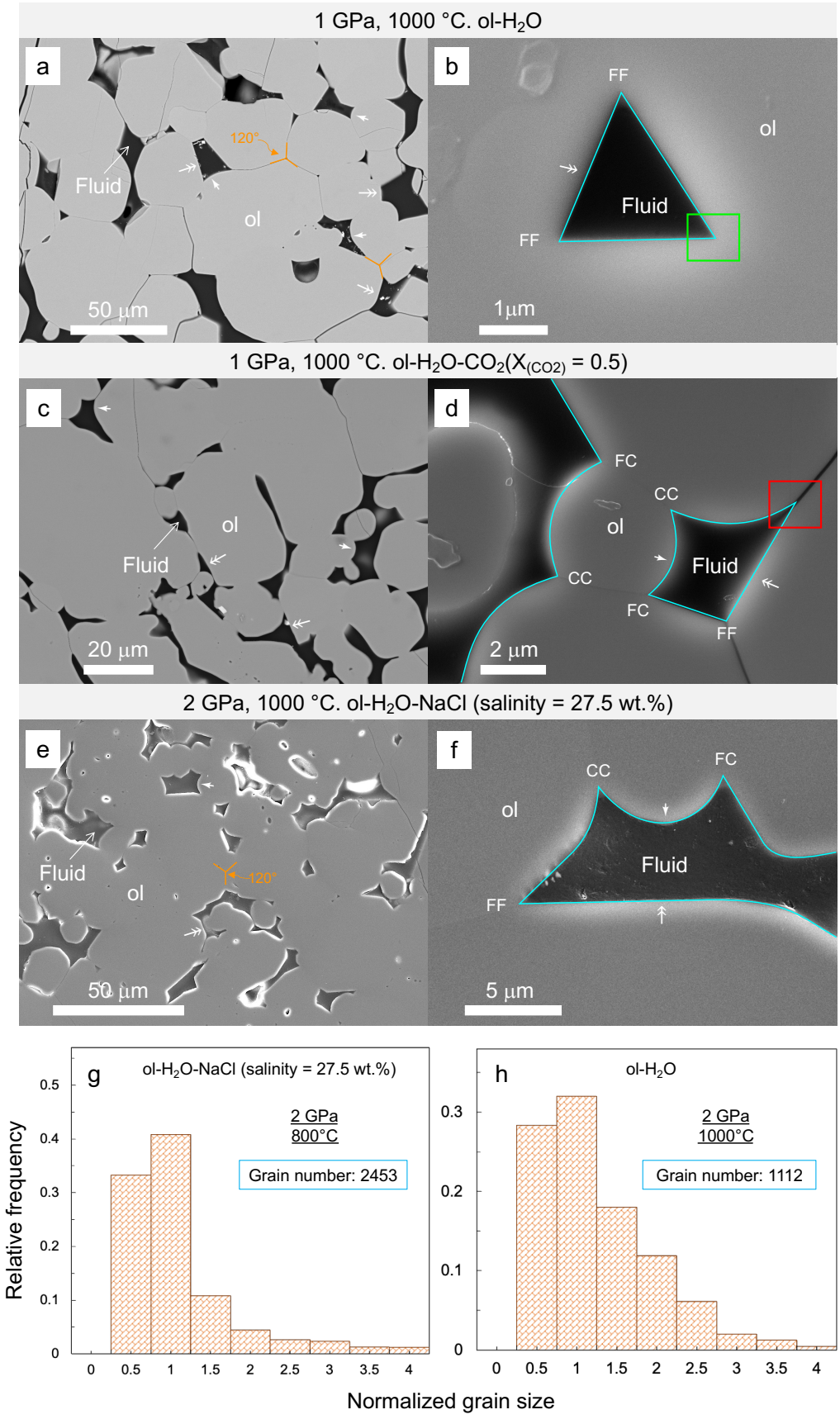
1 GPa, 1000 °C. ol-H2O
a
Fluid
120°
ol
50 μm
b
FF
ol
Fluid
FF
1μm
1 GPa, 1000 °C. ol-H2O-CO2(X(CO2) = 0.5)
c
ol
Fluid
20 μm
d
FC
CC
ol
Fluid
CC
FC
FF
2 μm
2 GPa, 1000 °C. ol-H2O-NaCl (salinity = 27.5 wt.%)
e
Fluid
ol
120°
50 μm
f
CC
FC
ol
Fluid
FF
5 μm
g
ol-H2O-NaCl (salinity = 27.5 wt.%)
2 GPa
800°C
Grain number: 2453
h
ol-H2O
2 GPa
1000°C
Grain number: 1112
Relative frequency
Normalized grain size

Figure 1. Representative SEM images and grain size distribution of the run products. a Backscattered electron image of the run product in the olivine–H_2O system at 1000°C and 1 GPa for 120 h. **b** High-magnification secondary electron image of a typical triple junction in the olivine–H_2O system at 1000°C and 1 GPa, which shows apparent FF angles. **c** Backscattered electron image of the run product in the H_2O–CO_2 system ($X_{(CO2)}$ = 0.5) at 1000°C and 1 GPa for 211 h. **d** High-magnification secondary electron image of the typical apparent θ in the H_2O–CO_2 system ($X_{(CO2)}$ = 0.5) at 1000°C and 1 GPa for 211 h, which shows the coexistence of three types of apparent θ. **e** Backscattered electron image of the run product in the H_2O–NaCl system (salinity = 27.5 wt.%) at 2 GPa and 1000°C for 120 h. **f** High-magnification secondary electron image of typical apparent θ in the H_2O–NaCl system (salinity = 27.5 wt.%) at 2 GPa and 1000°C for 120 h. The run products are composed of mineral grains and epoxy resin-filled pores previously filled with aqueous fluid during the experiment. The orange marks denote the olivine–olivine–olivine triple junctions with intersection angles of ~120°, indicating the attainment of textural equilibrium. The white single and double arrows represent the curved and faceted interfaces, respectively. For the CC, FC, FF angles, the interfaces in **b**, **d**, and **f** are highlighted by cyan curves. The green and red rectangles illustrate suitable and unsuitable angles (i.e., with a crack) for measurement, respectively. **g**, Histogram of the grain size distribution in the H_2O–NaCl system (salinity = 27.5 wt.%) at 2 GPa and 800°C. **h**, Histogram of the grain size distribution in the H_2O system at 2 GPa and 1000°C. The grain size distribution was normalized by the mean grain size of the recovered sample. The grain size is concentrated with a peak around the mean grain size. Abbreviations: ol = olivine, FF = faceted–faceted angle, FC = faceted–curved angle, CC= curved–curved angle.

3. Results

3.1. Product phases and microstructures

In all systems, the recovered samples are composed of olivine aggregates and intergranular fluid pores which are mostly filled with epoxy resin (Figure 1). The grain size of olivine in the run products increased with an enhancement of temperature, reaching ~110 μm at 1100°C through grain growth by Ostwald ripening and coalescence of two adjacent grains. The olivine grains were homogeneous in chemical compositions without obvious compositional zoning. Fluid-filled pores

were generally encompassed by three or more grains. Curved interfaces often coexisted with flat interfaces, even within a single pore (Figure 1). The curved interface results from the attainment of a constant mean curvature to minimize the surface energy by minimizing the surface area (Bargen & Waff, 1986; Waff & Faul, 1992), whereas the flat interface is attributed to the crystallographically controlled minimum interfacial energy (Yoshino et al., 2006). These two kinds of interfaces produce the three types of apparent θ: CC, FC, and FF (Figure 1b, d, and f). The attainment of local interfacial energy minimization via balancing of interfacial tensions at triple junctions (i.e., textural equilibration) was demonstrated by 1) the occurrence of many olivine triple junctions with angles of ~120° (Figure 1a, e) (e.g., Liu et al., 2018), 2) the cumulative frequency curves for apparent θ that shows good agreement with the predicted curve for an equilibrated texture (Elliott et al., 1997), and 3) the concentrated normalized grain size distribution on the mean grain size (Figure 1g, h; Figure S3 of the Supporting Information) (Faul, 1997; Huang et al., 2021). This is supported by the fact that the experimental durations (72–211 h) were sufficiently long for attaining textural equilibrium compared with those in previous studies (e.g., 12 h for a grain size of 10 μm at 727°C, Holness & Siklos, 2000). We measured the apparent FF and FC angles with clear interfaces (e.g., angles denoted by green rectangles in Figure 1b) and excluded those affected by cracks (e.g., the angle indicated by the red rectangle in Figure 1d).

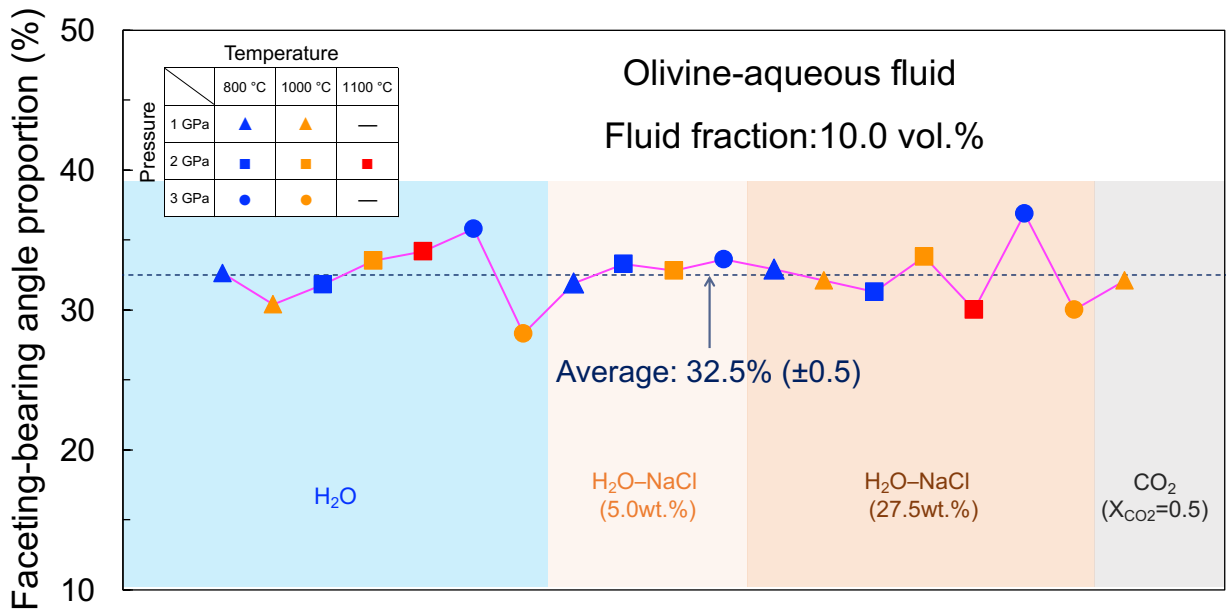

Figure 2. The faceting-bearing angle proportion measured from the olivine–fluid system. The results were calculated from 19 run products with a 10.0 vol.% fluid fraction. The average of 19 values is shown in the panel. The analytical error of each value is 0.5%. The P–T condition and fluid composition for each sample are shown in the panel.

3.2. Proportion of faceting-bearing angles

The proportion of facet-bearing angles (i.e., FF and FC angles) was evaluated from the SEM images of each recovered sample using Image–J (Figure 2). A total of 5025 angles were counted from the 19 samples (Table 1). To avoid the potential effect of heterogeneity in the angle–type distribution, we processed several images and obtained an average value for each sample. Although minor fluctuation occurs, the facet-bearing angle proportion is almost constant at approximately 32.5% (±0.5) without systematic P–T and fluid composition dependences. Namely, the FF and FC angles constituted approximately 1/3 of the dihedral angles. It is well demonstrated that the proportion of faceting is primarily controlled by ϕ and that the faceting proportion increases with an increase in the liquid fraction in the solid–liquid system (Watson & Lupulescu, 1993; Wark & Watson, 2000; Watson, 1999; Yoshino et al., 2005, 2006). Yoshino et al. (2005,

2006) reported that the faceting interface fraction in the olivine–basaltic melt system mostly fell in the range of 30.0–35.0 % with the melt fraction of 10.1–16.5 vol.%. Given an initial ϕ of approximately 10.0 vol.% in our study, our calculated faceting proportion is roughly consistent with the previous research (Yoshino et al., 2006).

3.3. Cumulative frequency of apparent dihedral angles

The representative cumulative frequencies of the measured FF and FC angles in the olivine–fluid systems at 2 GPa are shown in Figure 3, in which the curves of the apparent CC angles from Huang et al. (2019, 2020) are plotted for comparison. The rest of the cumulative frequencies for the other conditions and histograms for all systems in this study are shown in Figures S4 and S5 of the Supporting Information. For all systems investigated, the cumulative frequencies mostly showed a sharp enhancement around the median θ, and the frequency distribution histogram also showed a concentrated distribution of measured angles around the median value. In most cases, the CC angles sharply increase around the median angle, which is in accord with the theoretical prediction for the system with one true θ. In contrast, the FF angles gradually increased around the median angle. This could indicate the expanded range of true θ owing to surface energy anisotropy on the facet-bearing angles (Laporte & Provost, 2000). In some cases (Figure 3), the data largely deviated from the theoretical curve in regions of high apparent θ. This deviation was, first, attributed to the relatively small number of measured apparent FF angles. Second, this can be attributed to the presence of a very large θ associated possibly with sub-grain boundaries, in which the misorientation between two adjacent grains is very small (Laporte et al., 1997). These two possible reasons cause the FF and FC angles to deviate more from the theoretical

curve than CC angle. Nevertheless, the median angles in such cases are assumed to represent the true value because the angles smaller than the median fit the theoretical line well.

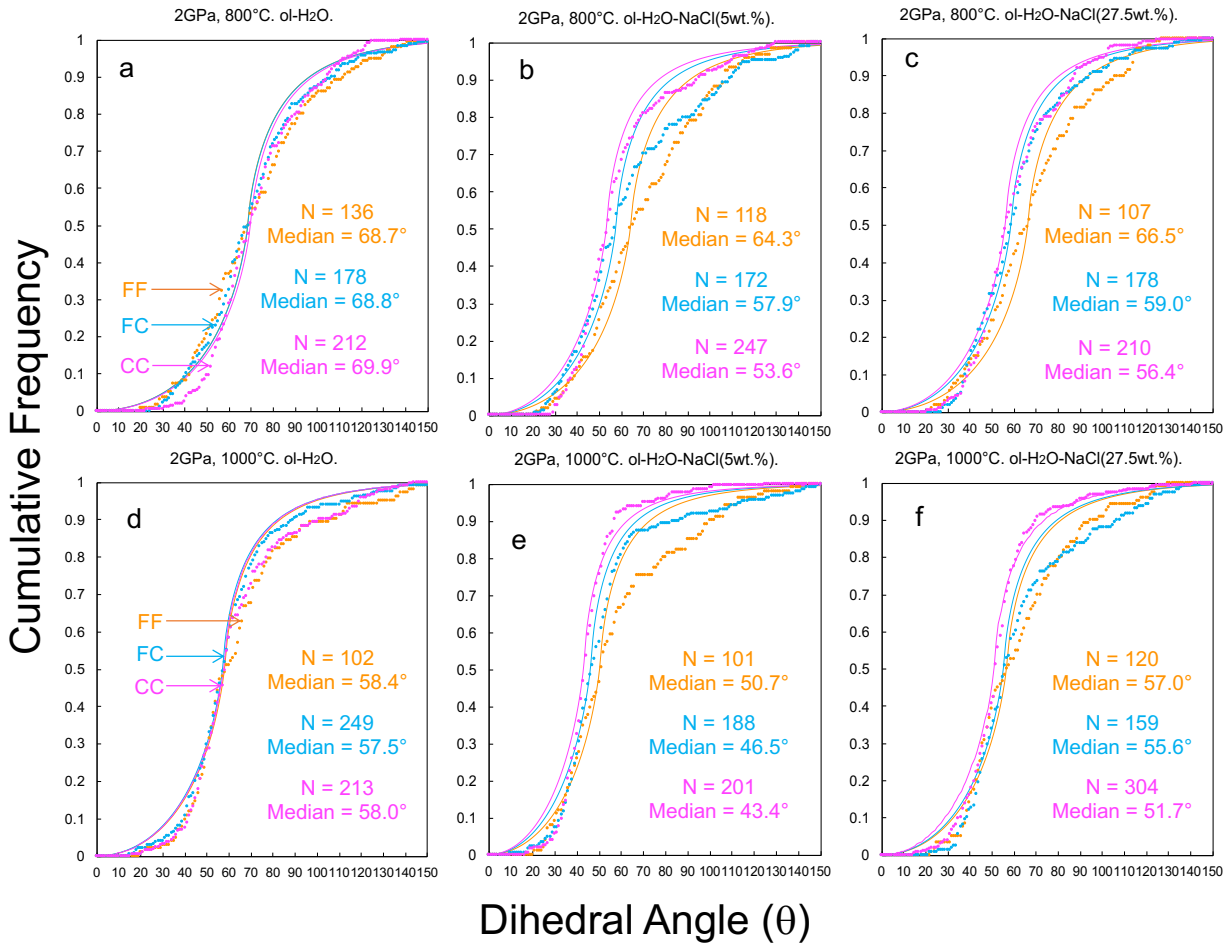

Figure 3. Representative cumulative frequency curves of measured apparent dihedral angles (θ) in olivine–fluid systems at 2 GPa and 800–1000 °C. The P–T condition and fluid composition are shown in the top of each panel. The facet-bearing angles (FC and FF) were measured in this study, while the data of the CC angles are from Huang et al. (2019, 2020). The median angle value and number (N) of the measured angles are shown for each case. The thin, solid curves represent the theoretical cumulative frequency curves obtained from the isotropic system with one true θ. Abbreviations: FF = faceted–faceted angle, FC = faceted–curved angle, CC = curved–curved angle.

3.4. Faceting effect on the median dihedral angle

The angle–type dependence of the median θ in the olivine–fluid systems at 1–3 GPa and 800–1100 °C is shown in Figure 4. Two angle–type dependencies were recognized according to the fluid compositions and P–T conditions. The angle values were comparable among the CC, FC, and FF in the H_2O systems at relatively low P–T conditions and the H_2O–CO_2 system. In contrast, the median angle of the facet-bearing angles was higher than that of the CC angle in the H_2O systems under higher P–T conditions and the H_2O–NaCl systems. Hereafter, the former and latter systems are called as I group (angle–type independent group) and D group (angle–type dependent group), respectively. The corresponding groups for each run product are summarized in Table 1. Under each P–T condition, FC and CC angles showed a relatively wide variation in θ between the H_2O and H_2O–NaCl systems, except for the results at 3 GPa and 1100°C, whereas FF angle was generally characterized by limited θ variations. The θ in the H_2O–CO_2 system at 1GPa and 1000°C was larger than those of the other fluid compositions irrespective of the angle–type. In the H_2O–NaCl (5.0 wt.% NaCl) systems, the θ values of the FF angle are similar (Figure 4a and c) or smaller by 5–10° than those in the H_2O and H_2O–NaCl (27.5 wt.% NaCl) systems at the same P–T conditions (Figure 4d and f).

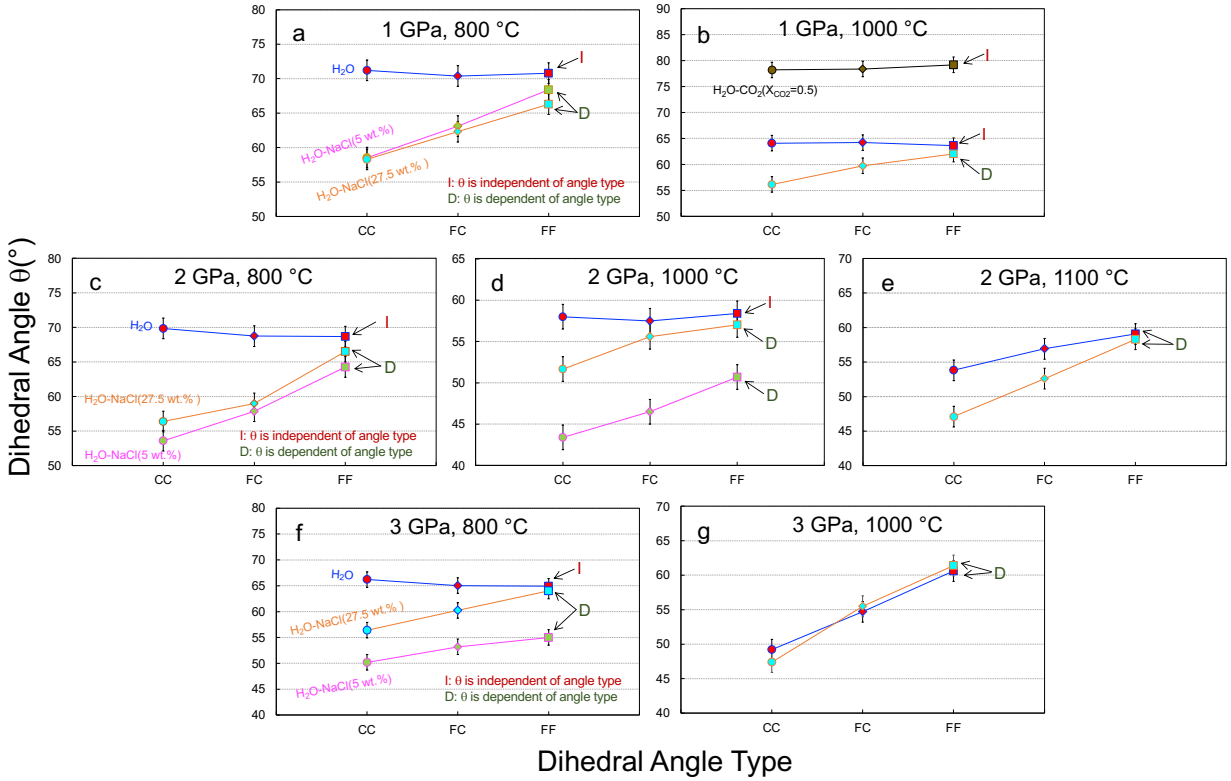

334

335 **Figure 4. Faceting dependence of the median dihedral angles (θ) in the olivine–fluid system at 1–3 GPa and**
336 **800–1100 °C.** Different colors in each panel denote the fluid compositions. The CC data are cited from Huang et al.
337 (2019, 2020). The error bar of ±1.5° is shown in the panels. Abbreviations: FF = faceted–faceted angle, FC = faceted–
338 curved angle, CC = curved–curved angle, I = angle–type independent group, D = angle–type dependent group.

339 **3.5. P–T dependence of the median dihedral angles in the different fluid systems**

340 The P–T dependence of the median FF and FC angle in the olivine–fluid systems measured
341 in this study is shown in Figure 5, along with the CC angle reported by Huang et al. (2019). The
342 CC angle decreases with increasing pressure and temperature (Figure 5c, f, and i), corresponding
343 to the increase in olivine solubility under high P–T conditions (Huang et al., 2019). On the other
344 hand, the P–T dependence of the FC and FF angles was not obvious compared to that of the CC
345 angle. In particular, the FF angles showed a stepwise change in θ but had similar θ values (Figure
346 5a, d, and g). These findings suggest that factors other than solubility variation dominantly

controlled θ of the FF angles. More discussion is given in Section 4.1 based on the EBSD results. It is worth noting that the median values of the FF angle were larger than, or close to, 60° in most cases.

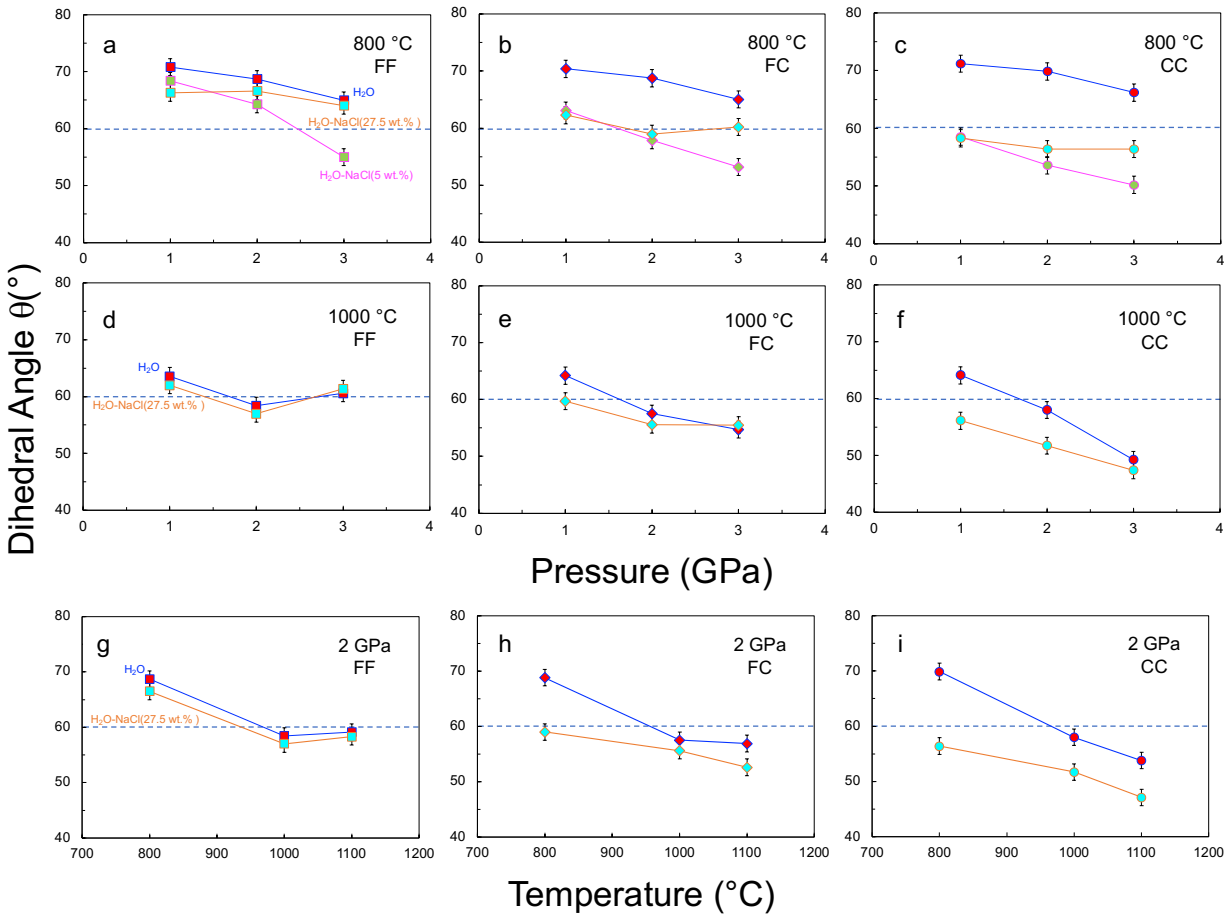

Figure 5. Pressure and temperature dependence of the median dihedral angles (θ) in the olivine–fluid system. **a–f** Pressure dependence at 800–1000 °C. **g–i**. Temperature dependence at 2 GPa. The P–T condition and fluid composition are shown in each panel. The CC data are from Huang et al. (2019). The error bar of ±1.5° is shown along with the median angle. The blue dash line represents θ of 60°. Abbreviations: FF = faceted–faceted angle, FC = faceted–curved angle, CC = curved–curved angle.

3.6. Crystallographic orientation of olivine

Figure 6 shows the representative EBSD maps and pole figures obtained from the five recovered samples. Figure S6 of the Supporting Information shows the rest of maps and pole figures. Our samples exhibited a merely weak (010) CPO (i.e., the *b* axis was slightly parallel to the compaction direction), regardless of the P–T conditions and fluid compositions. It was not as intense as the strong CPO that developed in the deformed olivine aggregate (Pommier et al., 2018). The weak CPO in this study is reasonable because the cell assembly of the piston–cylinder experiments with materials softened at high P–T conditions have been developed to avoid intense differential stress. Figure 7 shows the olivine grains' high-magnification orientation maps and the corresponding SE images. Additional figures related to the EBSD data processing are provided in Figures S7–S10 of the Supporting Information. If two adjacent grains have the same orientation, the apparent θ between the two grains will be large because of the small grain boundary energy (white circles in Figure 7a1–d1). Further analyses on the crystallographic orientations of the GBPs are described in the discussion.

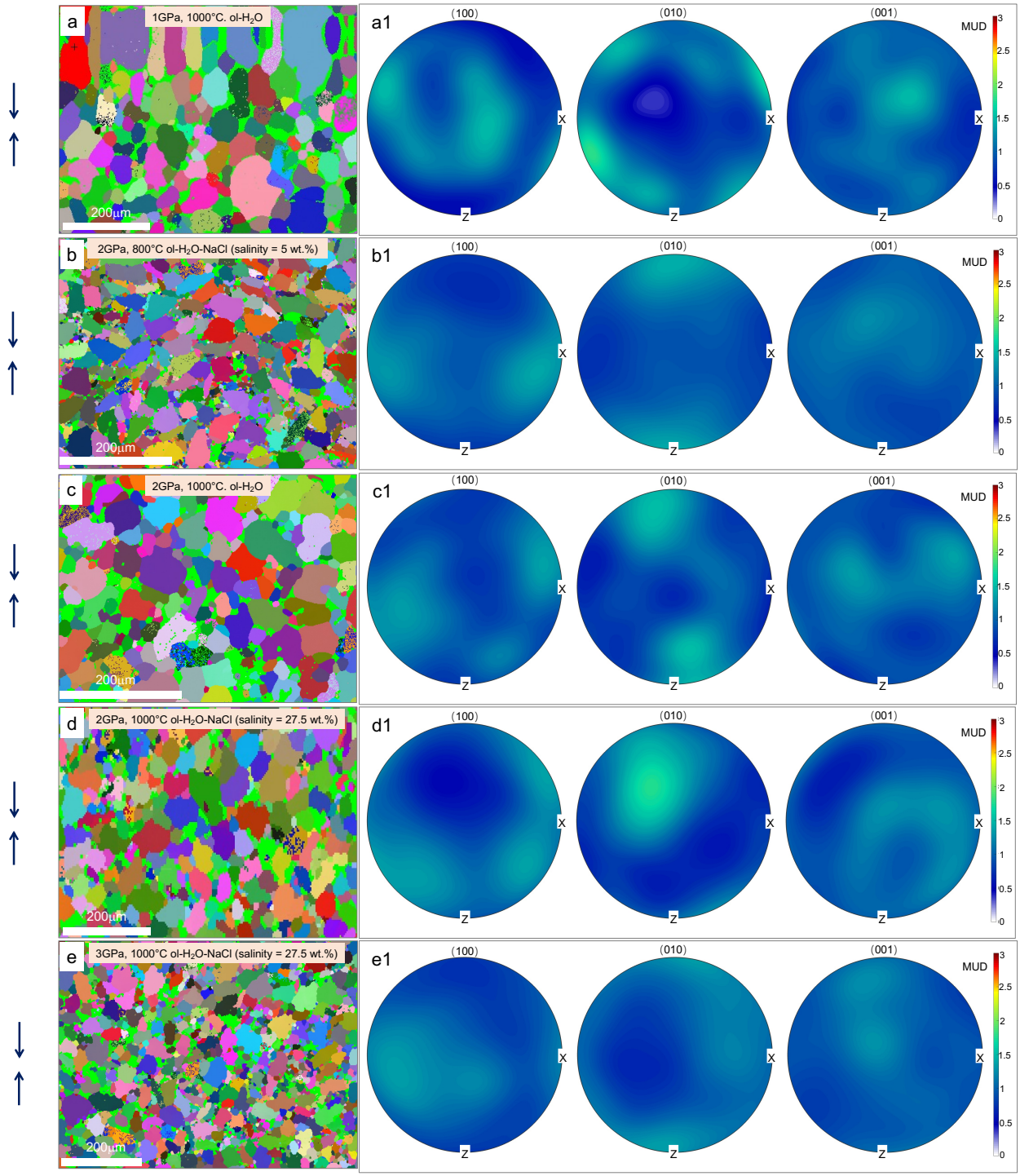

373

374 **Figure 6. Representative EBSD maps and corresponding pole figures. a–e**, EBSD maps of recovered olivine
375 aggregate in olivine–fluid systems. The small points within grains are attributed to the noise, crystal defects, and fluid
376 inclusions, which are mostly removed via denoise processes. In these systems, all grains are olivine with different
377 orientations. **a1–e1**, Pole figures to show the crystallographic orientations of (100), (010), and (001) corresponding to

a–e. The intensities in the color bar are multiples of the uniform distribution (MUD). The P–T condition and fluid composition are shown at the top of **a–e**. The arrow on the left side represents the compaction direction (parallel to the direction of piston movement).

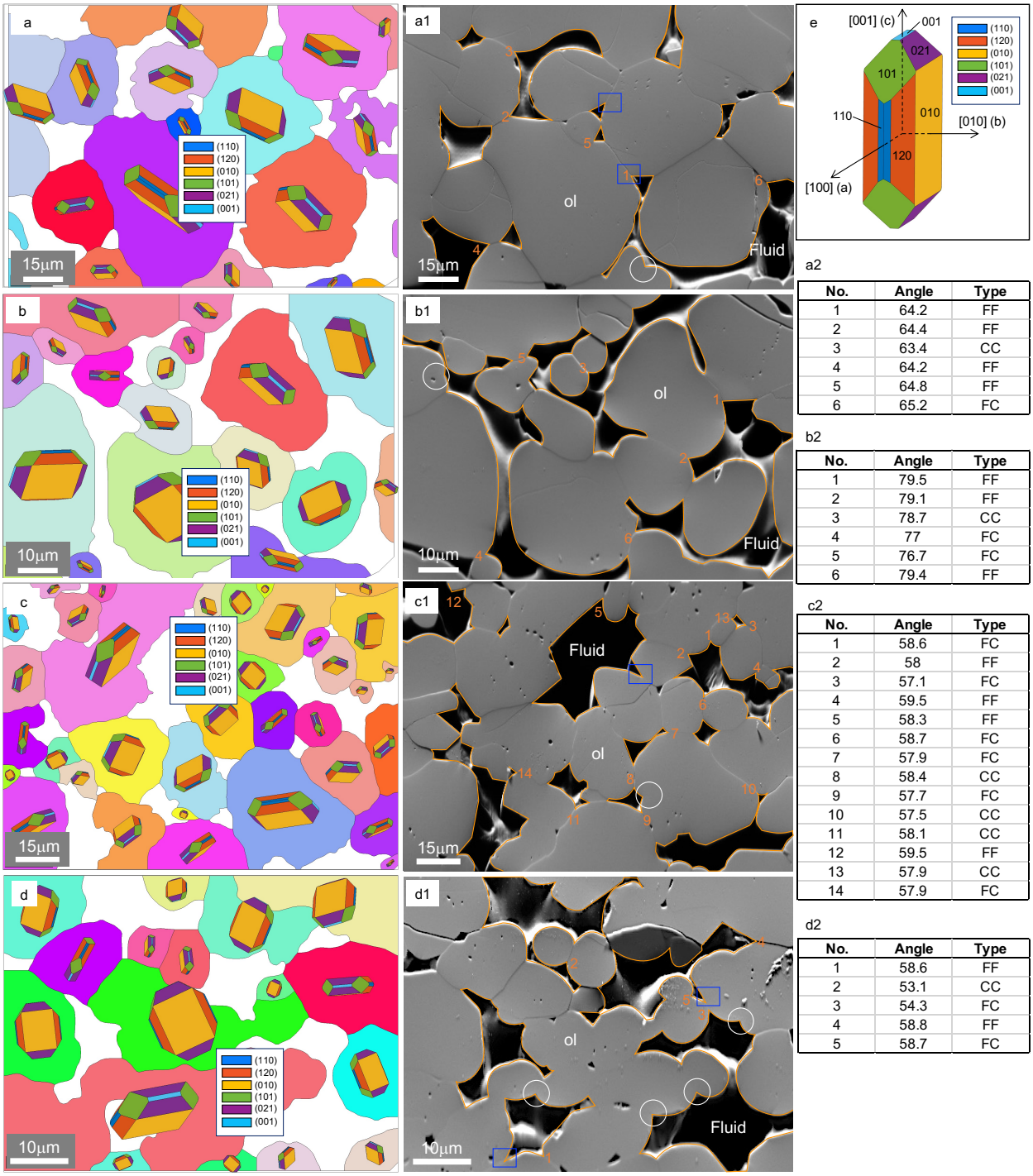

a2

No.	Angle	Type
1	64.2	FF
2	64.4	FF
3	63.4	CC
4	64.2	FF
5	64.8	FF
6	65.2	FC

b2

No.	Angle	Type
1	79.5	FF
2	79.1	FF
3	78.7	CC
4	77	FC
5	76.7	FC
6	79.4	FF

c2

No.	Angle	Type
1	58.6	FC
2	58	FF
3	57.1	FC
4	59.5	FF
5	58.3	FF
6	58.7	FC
7	57.9	FC
8	58.4	CC
9	57.7	FC
10	57.5	CC
11	58.1	CC
12	59.5	FF
13	57.9	CC
14	57.9	FC

d2

No.	Angle	Type
1	58.6	FF
2	53.1	CC
3	54.3	FC
4	58.8	FF
5	58.7	FC

Figure 7. The olivine grains' representative 3-D crystal orientation and corresponding SE image in the olivine–fluid system. EBSD mappings with 3-D crystal orientation of olivine in the H_2O system at 1 GPa and 1000°C **(a)**, in the H_2O–CO_2($X_{(CO2)}$=0.5) system at 1 GPa and 1000°C **(b)**, in the H_2O system at 2 GPa and 1000°C **(c)**, and in the H_2O–NaCl (27.5wt%) system at 2 GPa and 1000°C **(d)**. Colored and white areas denote olivine grains and fluid pools, respectively. The 3-D crystal orientation was visualized for each grain in the high magnification images by showing the oriented olivine crystal with an idealized morphology. Even though the grain configurations in **a–d** are slightly altered during EBSD data processes such as denoising and binarization, those essentially have no effects on the orientation identification. **e**, Crystal habit of single olivine crystal. **a1–d1**, Secondary electron images of recovered olivine aggregates corresponding to **a–d**. Olivine grains have a grey color, and fluid pools are black areas that are sometimes filled by resin. An orange outline visually emphasizes the interface between the olivine and fluids, and the apparent angles with a sequenced number are examples of analyzed angles and corresponding grain boundaries. **a2–d2**, Dihedral angle–types, and their values in terms of FF, FC, CC corresponding to measured angles in **a1–d1**. These angles have values close to the corresponding median θ. The white circle in **a1**–**d1** represents θ of two grains that have the same orientation, leading to a larger θ due to low misorientation of two adjacent grains. The blue square in a1, c1, and d1 represents θ that has one shared flat plane for both grain boundary and interfacial boundary. Abbreviations: ol = olivine, FF = faceted–faceted angle, FC = faceted–curved angle, CC = curved–curved angle.

3.7. Grain boundary plane distribution

To clarify the crystallographic orientation of olivine on GBPs, we evaluated the GBPD for the grain boundaries at the FF, FC, and CC angles on a high magnification orientation map (Figure 7). In general, GBPs are not vertical; they tend to incline at various degrees with respect to the polished cross-section of the sample. In the two-dimensional (2-D) SEM images, we cannot recognize how much these planes inclined. To mitigate this problem, we focused on the olivine–fluid–olivine triple junction with apparent dihedral angles lower than the median value + 5° and assumed that their grain boundaries were subvertical to the polished section. For example, in the system with one true θ of 60°, 71% of the apparent dihedral angles fell within the range from 0 to

65°, in which 68% of GBPs formed an angle greater than or equal to 67° with respect to the sectioning plane. Thus, we inferred the representative errors of ~23° in our GBPD analyses. More details about the errors of the GBPD analyses are provided in the Supporting Information Note 1 and Figures S1–S2. At such triple junctions, we determined the crystallographic orientations of olivine sharing the assumed vertical GBPs in the nine samples, including both I and D groups. In the calculation, we used the Euler angles derived from the EBSD analysis and the trend of the GBPs with respect to the horizontal side of the corresponding SEM image. The equivalent olivine orientations obtained for each angle–type were stereologically projected in the crystal reference frame, as shown in Figure 8.

In the I group, the low Miller Index planes such as (100) and (010) were dominant at the grain boundaries of the FF triple junctions, whereas the GBPs of the CC triple junctions were often characterized by a higher Miller Index such as (203). Note that the multiples of uniform density (MUD) spots indexed as (101) and (100) in Figure 8a1 are indistinguishable because of the tilt of the GBP. In the D group, the GBPs of the FF triple junctions were focused on (010), but equally around (130), which was interpreted as a broad concentration around (010). Although the differences in these planes were out of the possible errors of ± ~20° in our analyses, the large variations in the true θ at the FF angle especially in the D groups (Figure 3b, c, e, f, Section 3.3) could cause the apparent broadening of the concentration around (010) beyond the assumed errors. At the CC triple junctions, the high Miller Index planes around (130) is dominant, and the (100) is relatively weak. The GBPD at the FC triple junctions tended to exhibit mixed characteristics of the FF and CC results in both groups. Although the amount of the data was reduced, the GBPs at the faceted and curved sides were separately analyzed at the FC triple junctions, as shown in Figure 9. As in the FF and CC junctions, the GBPs at the faceted side were dominated by low Miller Index

planes such as (101) and (010), whereas the GBPs at the curved side rather preferred the high Miller Index planes such as (320) and (151). This indicates that the GBPDs observed in the FF and CC triple junctions are likely true. The weak CPO developed in the run products did not significantly affect the results.

Marquardt et al. (2015) found that the fluid-free olivine aggregates have a preferred (100) plane of the grain boundary, which is different from the preferential appearance of the (100), (010), and (101) planes on the grain boundaries at the FF angle in present study. This discrepancy is most likely due to the high ϕ in our study. The crystal habit of olivine grown freely in the fluid-rich system is characterized by the dominant (010) plane (Waff & Faul, 1992). Previous studies have shown that the (010) plane of olivine has the lowest energy, followed by the (100) and (001) planes in fluid/melt systems (Deer et al., 2013; Gurmani et al., 2011; de Leeuw et al., 2000; Watson et al., 1997), indicating a low grain boundary energy in the FF triple junctions.

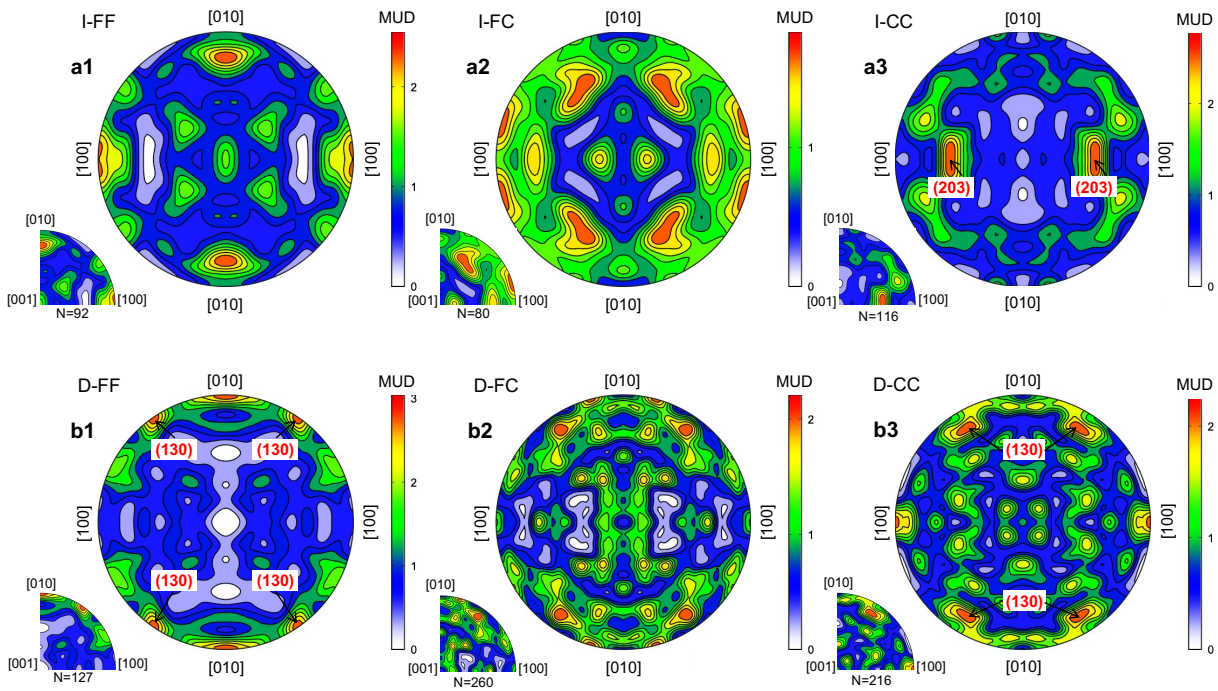

Figure 8. Pole figure of grain boundary plane distribution. a1–a3, Grain boundary plane distribution in the **I** group (i.e., the systems where the θ values are independent of the angle–type). **b1–b3,** Grain boundary plane distribution in the **D** group (i.e., the systems where the faceting increases θ). The equivalent olivine orientations obtained in the analysis were rearranged into the first quadrant to make the results more evident. Subsequently, by assuming that the grain boundary planes were equally distributed in each quadrant, the orientations in the first quadrant were copied in the other quadrants to obtain the pole figure. The analyzed number (N) in the first quadrant is shown at the lower left in each pole figure. MUD is the multiples of uniform density, shown by the color bar's intensities. The Miller Indexes were marked around the high MUD. Abbreviations: FF = faceted–faceted angle, FC = faceted–curved angle, CC = curved–curved angle, I = angle–type independent group, D = angle–type dependent group.

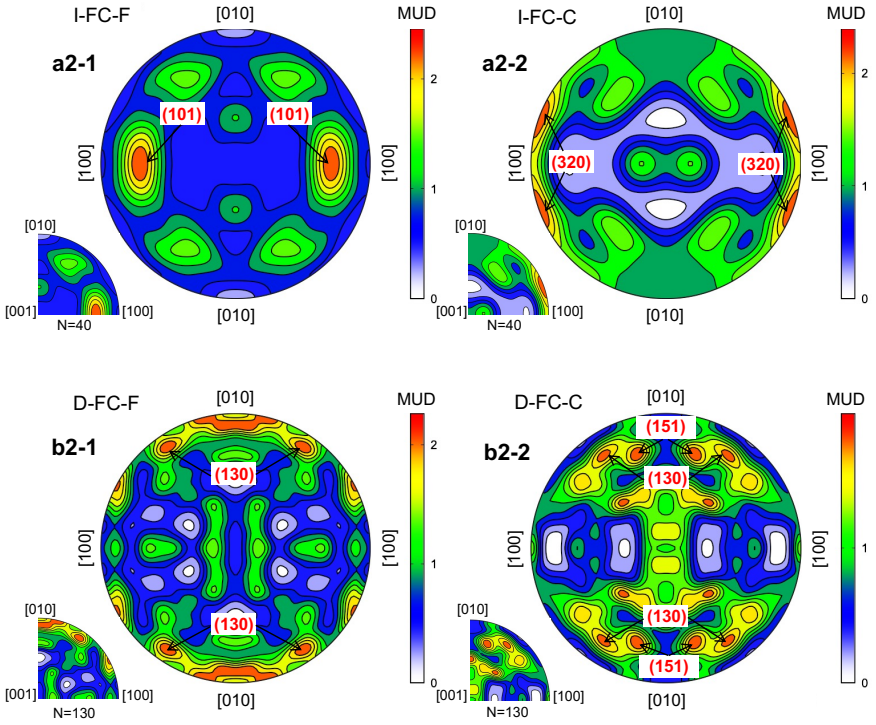

Figure 9. Pole figure of FC angles. Pole figure of grain boundary plane distributions (GBPDs) of faceted (**a2–1** and **b2–1**) and curved (**a2–2** and **b2–2**) sides at the FC triple junction for **I** group (i.e., the systems where the θ values are independent of the angle–type; **a2–1** and **a2–2**) and **D** group (i.e., the systems where the faceting increases θ; **b2–1** and **b2–2**). The data were plotted in the same way as in Figure 8. The analyzed number (N) in the first quadrant is shown at the lower left in each pole figure. MUD represents the multiples of uniform density, which shows the

intensities in the color bar. The Miller Indexes were marked around the high MUD. Abbreviations: FC = faceted–curved angle, F = grain boundary at the faceting side, C = grain boundary at the curved side, I = angle–type independent group, D = angle–type dependent group.

4. Discussion

In section 4.1, we calculated the theoretical FF angle based on the ideal crystal habit and discussed the primary factor controlling θ of FF angle. Based on our results, we further discuss the effect of the faceted interface on the fluid distribution under static conditions in Section 4.2 and the permeability anisotropy in the sheared mantle in Section 4.3.

4.1 Primary factor controlling θ of FF angle

Under high P–T conditions, enhanced olivine solubility significantly decreased the interfacial energy with the fluid, resulting in an obvious P–T dependence of θ of the CC angle (Huang et al., 2019, 2020). However, θ of the FF angle was less sensitive to P–T conditions than that of the CC angle, with discrete values. The variation cannot explain such characteristics in interfacial energy under P–T conditions. Laporte and Provost (2000) theoretically investigated an anisotropic system and showed that θ of the FF angle was controlled by the crystallographic orientation of two adjacent minerals. In this study, our GBPD analyses revealed that low Miller Index planes, such as (100), (010), and (101), preferentially appeared at the GBPs of the FF angle (Figures 8 and 9). Because the faceted mineral–fluid interfaces appeared to have low Miller indices, the θ value of the FF angle can be estimated from the angles between the GBPs of (100), (010), (101), and the other low Miller Index olivine surfaces. To test this inference, we calculated the angles between the GBPs of (100), (010), and (101) and the low-energy faceted planes of (001), (011), (110), (101), (120), and (021) based on the crystal planes appearing in the ideal habit of

olivine crystals (Figure. 7e). The calculations were made for asymmetrical configurations and symmetrical ones, because the olivine aggregate sintered in the present study showed a weak CPO (i.e., the random alignment of grains). Triple junctions that one extended grain boundary plane acts as one of interfaces, were considered as an extreme case (Flat face in Table 2). All the calculated configurations are presented in Table 1 of the Supporting Information and the angles consistent with the experimentally obtained FF θ (i.e., 50–55°, 55–65°, 65–70°, and 75–80°) are summarized in Table 2. The calculated candidates cover these experimental values in Table 2. For instance, the measured I–Type FF θ in the H_2O–CO_2 system at 1 GPa and 1000°C, is 79.2°. This may correspond to the calculated dihedral angles of 77.0° and 81.4° from a symmetrical triple junction composed of (100)–(101) and (010)–(021) planes, respectively, or 81.5°, 79.2°, and 80.1° from an asymmetrical triple junction composed of the (100)–(101) and (100)–(120), (010)–(021) and (100)–(101), and (101)–(120) and (100)–(110), respectively. In fact, the GBPs can be slightly inclined from the assumed planes, which may have resulted in a relatively broad distribution of the apparent FF θ as shown in Figure 4. For a symmetrical triple angle configuration, the two grains come in contact with the same low Miller index planes and share the lattice, whereas the lattice may not be highly shared for an asymmetrical triple angle configuration. The discrepancy in the grain boundary energy for these two cases is most likely negligible because the low Miller index GBPs have intrinsically low-surface energy (e.g., Yoshino et al., 2006). Thus, the θ value of the FC angle may be controlled by both interfacial energy and crystallographic orientation, resulting in the FC angle showing intermediate characteristics between the FF and CC angles.

505 **Table 2. Theoretical FF angle between two crystal planes**

Crystal	GBCP	IBCP	ACP(°)	Calculated FF Angle(°)	Configuration	Measured FF angle(°)
C1	100	110	25.0	50.0	Symmetrical	50–55
C2	100	110	25.0			
C1	101	001	51.5	51.5	Flat face	
C1	101	120	55.1	55.1	Flat face	
C1	100	110	25.0	63.5	Asymmetrical	55–65
C2	100	101	38.5			
C1	100	110	25.0	65.7	Asymmetrical	65–70
C2	100	021	40.7			
C1	101	021	66.2	66.2	Flat face	
C1	100	110	25.0	68.0	Asymmetrical	
C2	010	120	43.0			
C1	100	110	25.0	69.8	Asymmetrical	
C2	101	110	44.8			
C1	100	110	25.0	76.5	Asymmetrical	75–80
C2	101	110	51.5			
C1	100	101	38.5	77.0	Symmetrical	
C2	100	101	38.5			
C1	100	101	38.5	79.2	Asymmetrical	
C2	010	021	40.7			
C1	100	110	25.0	80.1	Asymmetrical	
C2	101	120	55.1			
C1	101	021	40.7	81.4	Symmetrical	
C2	101	021	40.7			
C1	100	101	38.5	81.5	Asymmetrical	
C2	100	120	43.0			

506
507
508 Note: The calculated FF angle was obtained by summing the two angles between two crystal planes (ACP). This
509 configuration shows the geometry of the calculated dihedral angle. We assume that the two crystals (crystal 1, C1;
510 crystal 2, C2) come in contact with same (symmetrical configuration) or different (asymmetrical configuration) low–
511 Miller index planes to form the FF angle. Additionally, we show extreme cases where one flat plane is shared for both
512 grain boundary and interfacial boundary. GBCP, grain boundary crystal plane; IBCP, interfacial boundary crystal
513 plane. The crystal cell parameters (a=4.7540 Å, b=10.1971 Å, and c=5.9806 Å) employed for the angle calculation
514 were obtained from Deer et al. (2013).

515

4.2. Consequences of faceting on the fluid connectivity in the undeformed olivine–fluid system

Our study demonstrated that ~1/3 of the dihedral angles in the olivine–fluid system are facet-bearing, irrespective of P–T conditions and fluid compositions (Table 1). The fluid pores surrounded by faceted interfaces are difficult to connect each other even at $\theta < 60°$, which requires a threshold ϕ for the establishment of a fluid network, as in the case of a CC angle > 60° (Price et al., 2006). Thus, a system that includes both curved and faceted interfaces with low ϕ, the bulk permeability may be reduced. Huang et al. (2021) measured the electrical conductivity of the fluid-bearing forsterite aggregate with various ϕ under the textural equilibrium states at 1 GPa and 800°C in the H_2O–NaCl system with 5.0 wt.% NaCl. The electrical conductivity measurements and the synchrotron X–ray computed CT imaging of the post run products showed that fluid pores were not interconnected at ϕ of 0.51 vol.%. In contrast, they started to form the fluid network at ϕ above 2.14 vol.%. Although the CC angle can be lower than 60° under this experimental P–T condition (Huang et al., 2019), fluid interconnection was not established at ϕ below ~1.0–2.0 vol.%. This could most likely be attributed to a presence of substantial number of faceted interfaces that increases ϕ_c and decreases the permeability, as pointed out by Price et al. (2006).

Toramaru and Fujii (1986) examined the melt connectivity in peridotites composed of olivine, clinopyroxene, and orthopyroxene based on a bond percolation model with the melt stability at the grain edges and corners, namely, dihedral angles. They found that the partial melt was not stable at pyroxene-dominated grain edges and that the interconnection was established when pyroxene modal composition was lower than ~25–20 vol.% when the grain size of olivine and pyroxenes are similar. If we assume that the faceting triple junctions hampers the fluid

interconnection, an analogous discussion will be possible for the fluid connectivity in facet-bearing olivine aggregates. Given the slightly higher proportion of faceting triple junctions (28–36%; Table 1) than the above pyroxene modal composition of Toramaru and Fujii (1986), the electrical conductivity results of Huang et al. (2021), in which the fluid percolation was prohibited at ϕ=0.51 vol.% but established at a small critical fraction (2.14 vol.%) seems consistent with the model prediction.

4.3. Preferential appearance of faceted fluid pores in the sheared mantle

Our study demonstrated that faceted olivine–fluid interfaces are preferentially accompanied by low Miller index GBPs such as (100), (010), and (101). The extensive occurrence of faceted crystallographic faces in deep-seated rocks can change the bulk permeability, elastic, anelastic, and electrical properties (Waff & Faul, 1992). Waff and Faul (1992) investigated the melt distribution in the texturally equilibrated olivine–melt system and found that the presence of the melt film along the pervasive faceted crystal interface was making θ much smaller, and increasing the permeability of the bulk rock. However, the effect of the faceted interface on pore morphology and permeability obtained from olivine–fluid systems in the present study is different from that of olivine–melt system. Our results showed that the grain boundaries associated to the flat interface are dry and the FF and FC θ were comparable to or larger than the CC angles, working against the establishment of fluid connectivity. This effect could be magnified under the shear stress such as the corner flow in subduction zones. In the deformed olivine aggregate with strong CPO, the crystal axes (i.e., *a*, *b*, and *c* axes) of olivine grains are aligned in specific directions depending on the temperature, olivine water content, and stress state (Jung et al., 2006; Jung & Karato, 2001; Karato et al., 2008; Kneller et al., 2005, 2008). This alignment may lead to low

560 Miller index planes dominating grain boundaries, thereby increasing the proportion of facet-
561 bearing angles in the sheared mantle.

562 Jung and Karato (2001) examined the water-saturated olivine fabric under shear strain and
563 found that the c axis was subparallel to the shear direction, and the b axis was perpendicular to the
564 shear direction (B–type fabric). Therefore, in water-rich subduction zone, a B–type fabric is
565 expected, in which the c axis is subparallel to the subduction direction and the b axis is
566 perpendicular to the plate interface. Liu and Zhao (2017) detected the Vp anisotropy in the mantle
567 wedge beneath Japan, supporting the hypothesis that the B–type fabric is dominant in the fore-arc
568 mantle wedge. This type of grain alignment could produce abundant grain boundaries composed
569 of the (100) and (010) planes parallel to the subduction direction to form many FF angles
570 comparable to or larger than the CC angle, decreasing the permeability and electrical conductivity
571 along the subduction direction. That is to say, the presence of faceting may contribute to the
572 anisotropy of permeability and conductivity, which is important for understanding fluid flow, flux
573 melting, anomalies of the electrical conductivity, and seismic wave velocities in subduction
574 systems.

575 ## 5. Conclusion

576 In this study, we determined quantitatively the effect of faceting on the olivine–fluid θ in
577 different fluid systems (H_2O, H_2O–CO_2 ($X_{(CO2)}$ = 0.5), H_2O–NaCl (5.0 and 27.5 wt.% NaCl)) at 1–
578 3 GPa and 800–1100 °C. The results show that 1/3 of olivine–fluid θ are faceted plane-bearing
579 angles irrelative to the P–T conditions and fluid compositions. The θ measurement shows that in
580 the H_2O systems at relatively low P–T conditions and in the H_2O–CO_2 system, the facet-bearing
581 angle values (i.e., FF, FC) are comparable to those of the CC angle. However, in the H_2O systems

582 at high P–T conditions and in the H_2O–NaCl systems, the facet-bearing angle values (i.e., FF, FC)
583 are larger than those of the CC angle. EBSD analyses show that the run products do not have an
584 intense crystallographic preferred orientation (CPO) corresponding to static compression
585 conditions. Strikingly, the grain boundary plane distribution (GBPD) revealed that the faceted and
586 curved interfaces at facet-bearing triple junctions have grain boundary planes (GBPs) subjected to
587 the low (e.g., (100), (010), (101)) and high (e.g., (130), (203), (320)) Miller Index faces,
588 respectively. The calculation of θ values between two adjacent crystal planes highly reproduces
589 the measured values of the FF angles, which further supports the results of our GBPD analyses.
590 Therefore, our results suggest the importance of crystallographic orientation in determine the
591 origin of the FF angle. The presence of the FF angle and associated changes in fluid pore
592 morphology will require a high fluid fraction for establishing the fluid networks. It will further
593 lead to the permeability anisotropy and changes in geophysical characteristics, particularly for the
594 mantle wedge settings where olivine CPO is expected.

595 ## Acknowledgments

596 This work was supported by JSPS KAKENHI Grant Nos. JP16H06348 and JP16K13903
597 awarded to M. Nakamura, JSPS Japanese–German Graduate Externship, International Joint
598 Graduate Program in Earth and Environmental Sciences, Tohoku University (GP–EES), and by
599 the Ministry of Education, Culture, Sports, Science and Technology (MEXT) of Japan under its
600 Earthquake and Volcano Hazards Observation and Research Program, the Core Research Cluster
601 of Disaster Science in Tohoku University (Designated National University), and by the
602 Tuguangchi Award for Excellent Young Scholar (E1510316) in Guangzhou Institute of
603 Geochemistry, Chinese Academy of Sciences. We provide the datasets on figshare
604 (https://doi.org/10.6084/m9.figshare.19786252.v1), including dataset of pole figure derived from
605 EBSD data and dataset of FF angle calculation, to support our research.

606

Reference

Allen, C., J. (1972). The role of water in the mantle of the earth: the stability of amphiboles and micas. *24th International Geological Congress, Montreal*, *2*, 231–240.

Angiboust, S., Pettke, T., de Hoog, J. C. M., Caron, B., & Oncken, O. (2014). Channelized Fluid Flow and Eclogite-facies Metasomatism along the Subduction Shear Zone. *Journal of Petrology*, *55*(5), 883–916. https://doi.org/10.1093/PETROLOGY/EGU010

Cmíral, M., Fitz Gerald, J. D., Faul, U. H., & Green, D. H. (1998). A close look at dihedral angles and melt geometry in olivine–basalt aggregates: A TEM study. *Contributions to Mineralogy and Petrology*, *130*(3–4), 336–345. https://doi.org/10.1007/s004100050369

de Leeuw, N. H., Parker, S. C., Catlow, C. R. A., & Price, G. D. (2000). Modelling the effect of water on the surface structure and stability of forsterite. *Physics and Chemistry of Minerals, 27*, 332–341. https://doi.org/10.1007/S002690050262

Deer et al. (2013). An Introduction to the Rock-Forming Minerals (third edition). *The Canadian Mineralogist*, *51*. https://doi.org/10.3749/CANMIN.51.4.663

Elliott, M. T., Cheadle, M. J., & Jerram, D. A. (1997). On the identification of textural equilibrium in rocks using dihedral angle measurements. *Geology*, *25*(4), 355–358. https://doi.org/10.1130/0091–7613

Faul, U. H. (1997). Permeability of partially molten upper mantle rocks from experiments and percolation theory. *Journal of Geophysical Research: Solid Earth*, *102*(B5), 10299–10311. https://doi.org/10.1029/96jb03460

Faul, U. H., & Fitz Gerald, J. D. (1999). Grain misorientations in partially molten olivine aggregates: an electron backscatter diffraction study. *Physics and Chemistry of Minerals*, *26*(3), 187–197. https://doi.org/10.1007/S002690050176

Gurmani, S. F., Jahn, S., Brasse, H., & Schilling, F. R. (2011). Atomic scale view on partially molten rocks: Molecular dynamics simulations of melt-wetted olivine grain boundaries. *Journal of Geophysical Research: Solid Earth*, *116*(B12), 12209. https://doi.org/10.1029/2011JB008519

Hermann, J., Spandler, C., Hack, A., & Korsakov, A. v. (2006). Aqueous fluids and hydrous melts in high–pressure and ultra-high pressure rocks: Implications for element transfer in subduction zones. *Lithos*, *92*(3–4), 399–417. https://doi.org/10.1016/j.lithos.2006.03.055

Holness, M. B., & Siklos, S. T. C. (2000). The rates and extent of textural equilibration in high–temperature fluid–bearing systems. *Chemical Geology*, *162*, 137–153. https://doi.org/10.1016/S0009–2541(99)00124–2

Holness, M. B. (1992). Equilibrium dihedral angles in the system quartz–CO_2–H_2O–NaCl at 800°C and 1–15 kbar: the effects of pressure and fluid composition on the permeability of quartzites. *Earth and Planetary Science Letters*, *114*(1), 171–184. https://doi.org/10.1016/0012–821X(92)90159–S

644 Holness, M. B. (1993). Temperature and pressure dependence of quartz–aqueous fluid dihedral
645 angles: the control of adsorbed H_2O on the permeability of quartzites. *Earth and Planetary*
646 *Science Letters*, *117*(3–4), 363–377. https://doi.org/10.1016/0012–821X(93)90090–V
647 Huang, Y., Nakatani, T., Nakamura, M., & McCammon, C. (2019). Saline aqueous fluid
648 circulation in mantle wedge inferred from olivine wetting properties. *Nature Communications*,
649 *10*(1), 5557. https://doi.org/10.1038/s41467–019–13513–7
650 Huang, Y., Nakatani, T., Nakamura, M., & McCammon, C. (2020). Experimental constraint on
651 grain–scale fluid connectivity in subduction zones. *Earth and Planetary Science Letters*, *552*,
652 116610. https://doi.org/10.1016/j.epsl.2020.116610
653 Huang, Y., Guo, H., Nakatani, T., Uesugi, K., Nakamura, M., & Keppler, H. (2021). Electrical
654 Conductivity in Texturally Equilibrated Fluid–Bearing Forsterite Aggregates at 800°C and
655 1 GPa: Implications for the High Electrical Conductivity Anomalies in Mantle Wedges.
656 *Journal of Geophysical Research: Solid Earth*, *126*(4), e2020JB021343.
657 https://doi.org/10.1029/2020JB021343
658 Iwamori, H. (1998). Transportation of H_2O and melting in subduction zones. *Earth and Planetary*
659 *Science Letters*, *160*(1–2), 65–80. https://doi.org/10.1016/S0012–821X(98)00080–6
660 Jung, H., & Karato, S. I. (2001). Water-Induced Fabric Transitions in Olivine. *Science*, *293*(5534),
661 1460–1463. https://doi.org/10.1126/SCIENCE.1062235
662 Jung, H., Katayama, I., Jiang, Z., Hiraga, T., & Karato, S. (2006). Effect of water and stress on the
663 lattice–preferred orientation of olivine. *Tectonophysics, 421*, 1–22.
664 https://doi.org/10.1016/j.tecto.2006.02.011
665 Jurewicz, S. R., & Jurewicz, A. J. G. (1986). Distribution of apparent angles on random sections
666 with emphasis on dihedral angle measurements. *Journal of Geophysical Research*, *91*(B9),
667 9277. https://doi.org/10.1029/jb091ib09p09277
668 Karato, S. I., Jung, H., Katayama, I., & Skemer, P. (2008). Geodynamic Significance of Seismic
669 Anisotropy of the Upper Mantle: New Insights from Laboratory Studies. *Annual Review of*
670 *Earth and Planetary Sciences*, *36*, 59–95.
671 https://doi.org/10.1146/ANNUREV.EARTH.36.031207.124120
672 van Keken, P. E., Hacker, B. R., Syracuse, E. M., & Abers, G. A. (2011). Subduction factory: 4.
673 Depth-dependent flux of H_2O from subducting slabs worldwide. *Journal of Geophysical*
674 *Research*, *116*(B1), B01401. https://doi.org/10.1029/2010JB007922
675 von Bargen, N., & Waff, H. S. (1986). Permeabilities, interfacial areas and curvatures of partially
676 molten systems: Results of numerical computations of equilibrium microstructures. *Journal*
677 *of Geophysical Research*, *91*(B9), 9261. https://doi.org/10.1029/JB091IB09P09261
678 Kneller, E. A., van Keken, P. E., Karato, S. I., & Park, J. (2005). B–type olivine fabric in the
679 mantle wedge: Insights from high-resolution non-Newtonian subduction zone models. *Earth*
680 *and Planetary Science Letters*, *237*(3–4), 781–797.
681 https://doi.org/10.1016/J.EPSL.2005.06.049

Kneller, E. A., Long, M. D., & van Keken, P. E. (2008). Olivine fabric transitions and shear wave anisotropy in the Ryukyu subduction system. *Earth and Planetary Science Letters*, *268*, 268–282. https://doi.org/10.1016/j.epsl.2008.01.004

Laporte, D., & Provost, A. (2000). Equilibrium geometry of a fluid phase in a polycrystalline aggregate with anisotropic surface energies: Dry grain boundaries. *Journal of Geophysical Research: Solid Earth*, *105*(B11), 25937–25953. https://doi.org/10.1029/2000jb900256

Laporte, D., & Watson, E. B. (1995). Experimental and theoretical constraints on melt distribution in crustal sources: the effect of crystalline anisotropy on melt interconnectivity. *Chemical Geology*, *124*(3–4). https://doi.org/10.1016/0009–2541(95)00052–N

Laporte, D., Rapaille, C. and Provost, A., (1997). Wetting angles, equilibrium melt geometry, and the permeability threshold of partially molten crustal protoliths. *In Granite: from segregation of melt to emplacement fabrics*, 31–54. Springer, Dordrecht. https://doi.org/10.1007/978–94–017–1717–5–3

Liu, X., & Zhao, D. (2017). P-wave anisotropy, mantle wedge flow and olivine fabrics beneath Japan. *Geophysical Journal International*, *210*, 1410–1431. https://doi.org/10.1093/GJI/GGX247

Liu, X., Matsukage, K.N., Li, Y., Takahashi, E., Suzuki, T., & Xiong, X., (2018). Aqueous Fluid Connectivity in Subducting Oceanic Crust at the Mantle Transition Zone Conditions. *Journal of Geophysical Research: Solid Earth*, *123*, 6562–6573 https://doi.org/10.1029/2018JB015973

Marquardt, K., Rohrer, G. S., Morales, L., Rybacki, E., Marquardt, H., & Lin, B. (2015). The most frequent interfaces in olivine aggregates: the GBCD and its importance for grain boundary related processes. *Contributions to Mineralogy and Petrology*, *170*(4), 1–17. https://doi.org/10.1007/S00410–015–1193–9

Médard, E., McCammon, C. A., Barr, J. A., & Grove, T. L. (2008). Oxygen fugacity, temperature reproducibility, and H_2O contents of nominally anhydrous piston–cylinder experiments using graphite capsules. *American Mineralogist*, *93*(11–12), 1838–1844. https://doi.org/10.2138/am.2008.2842

Mibe, K., Fujii, T., & Yasuda, A. (1998). Connectivity of aqueous fluid in the Earth's upper mantle. *Geophysical Research Letters*, *25*(8), 1233–1236. https://doi.org/10.1029/98GL00872

Mibe, K., Fujii, T., & Yasuda, A. (1999). Control of the location of the volcanic front in island arcs by aqueous fluid connectivity in the mantle wedge. *Nature*, *401*(6750), 259–262. https://doi.org/10.1038/45762

Pommier, A., & Evans, R. L. (2017). Constraints on fluids in subduction zones from electromagnetic data. *Geosphere*, *13*(4), 1026–1049. https://doi.org/10.1130/GES01473.1

Pommier, A., Kohlstedt, D. L., Hansen, L. N., Mackwell, S., Tasaka, M., Heidelbach, F., & Leinenweber, K. (2018). Transport properties of olivine grain boundaries from electrical conductivity experiments. *Contributions to Mineralogy and Petrology*, *173*(5), 41. https://doi.org/10.1007/s00410–018–1468–z

Price, J. D., Wark, D. A., Watson, E. B., & Smith, A. M. (2006). Grain-scale permeabilities of faceted polycrystalline aggregates. *Geofluids*, *6*(4), 302–318. https://doi.org/10.1111/j.1468–8123.2006.00149.x

Toramaru, A., & Fujii, N. (1986). Connectivity of melt phase in a partially molten peridotite. *Journal of Geophysical Research: Solid Earth*, *91*(B9), 9239–9252. https://doi.org/10.1029/JB091IB09P09239

Waff, H. S., & Faul, U. H. (1992). Effects of crystalline anisotropy on fluid distribution in ultramafic partial melts. *Journal of Geophysical Research*, *97*(B6), 9003. https://doi.org/10.1029/92JB00066

Wark, D. A., & Watson, E. B. (2000). Effect of grain size on the distribution and transport of deep–seated fluids and melts. *Geophysical Research Letters*, *27*(14), 2029–2032. https://doi.org/10.1029/2000GL011503

Watson, E., & Brenan, J. M. (1987). Fluids in the lithosphere, 1. Experimentally-determined wetting characteristics of CO_2–H_2O fluids and their implications for fluid transport, host-rock physical properties, and fluid inclusion formation. *Earth and Planetary Science Letters*, *85*(4), 497–515. https://doi.org/10.1016/0012–821X(87)90144–0

Watson, E., & Lupulescu, A. (1993). Aqueous fluid connectivity and chemical transport in clinopyroxene-rich rocks. *Earth and Planetary Science Letters*, *117*(1–2), 279–294. https://doi.org/10.1016/0012–821X(93)90133–T

Watson, E., (1999). Lithogic partitioning of fluids and melts. *American Mineralogist*, *84*(11–12), 1693–1710. https://doi.org/10.2138/AM–1999–11–1201

Watson, G. W., Oliver, P. M., & Parker, S. C. (1997). Computer simulation of the structure and stability of forsterite surfaces. *Physics and Chemistry of Minerals*, *25*(1), 70–78. https://doi.org/10.1007/S002690050088

Worzewski, T., Jegen, M., Kopp, H., Brasse, H., & Taylor Castillo, W. (2011). Magnetotelluric image of the fluid cycle in the Costa Rican subduction zone. *Nature Geoscience*, *4*(2), 108–111. https://doi.org/10.1038/ngeo1041

Yoshino, T., Takei, Y., Wark, D. A., & Watson, E. B. (2005). Grain boundary wetness of texturally equilibrated rocks, with implications for seismic properties of the upper mantle. *Journal of Geophysical Research: Solid Earth*, *110*(B8), 1–16. https://doi.org/10.1029/2004JB003544

Yoshino, T., Price, J. D., Wark, D. A., & Watson, E. B. (2006). Effect of faceting on pore geometry in texturally equilibrated rocks: implications for low permeability at low porosity. *Contributions to Mineralogy and Petrology, 152*(2), 169–186. https://doi.org/10.1007/S00410–006–0099–Y

Zheng, Y. F., Chen, R. X., Xu, Z., & Zhang, S. B. (2016). The transport of water in subduction zones. *Science China Earth Sciences*, *59*, 651–682. https://doi.org/10.1007/s11430–015–5258–4

Journal of Geophysical Research: Solid Earth

Supporting Information for

The effect of faceting on olivine wetting properties

Yongsheng Huang[1, a*], Takayuki Nakatani[1, b], Sando Sawa[1, c], Michihiko Nakamura[1], Catherine McCammon[2]

1. Department of Earth Science, Graduate School of Science, Tohoku University, Aramaki–Aza–Aoba, Aoba–Ku, Sendai, Miyagi 980–8578, Japan

2. Bayerisches Geoinstitut, University of Bayreuth, 95440 Bayreuth, Germany

a. Current address: Guangzhou Institute of Geochemistry, Chinese Academy of Sciences, 511 Kehua Street, Wushan, Tianhe, Guangzhou 510640, China.

b. Current address: Geological Survey of Japan, AIST Central 7, Higashi 1–1–1, Tsukuba, Ibaraki 305–8567, Japan.

c. Current address: Division of Advanced Mechanical Systems Engineering, Institute of Engineering, Tokyo University of Agriculture and Technology, Nakamachi 2-24-16, Koganei, Tokyo, 184-0012, Japan.

* Corresponding author. Email: huangyongsheng@gig.ac.cn

Contents of this file

1. Note 1. Errors of the GBPD analyses

Our GBPD analyses focused on the olivine–olivine–fluid triple junction with apparent dihedral angles lower than the median value + 5° and assumed a vertical grain boundary plane there. Based on the simple theoretical calculation, we show that grain boundary planes at such triple junctions are

dominantly subvertical with respect to the polished section. Although we cannot exactly determine the extent of grain boundary plane tilting in the cross-sectional image, the apparent dihedral angles can be used to constrain the extent of tilting statistically.

Following the method of Harker and Parker (1945), we can calculate e apparent dihedral angle, Y on an arbitrary sectioning plane at the mineral–mineral–fluid triple junction in an isotropic system with one true dihedral angle θ. This method is identical to that used to compute the theoretical cumulative frequency curve of the apparent dihedral angle, as shown in Figure 3. A schematic of the triple junction with a sectioning plane is shown in Figure S1. The unit normal of the sectioning plane is defined in angular coordinates Q and ϕ (Q, ϕ = 0–90°), and Y is a function of θ, Q, and ϕ (Harker & Parker, 1945). In Figure S2a, the contours of Y for a representative θ of 60° are shown in the sin2Q versus ϕ diagram. In this diagram, the area fraction of angles ≤ Y corresponds to the probability that the observed apparent dihedral angles become less than, or equal to, Y (Harker & Parker, 1945). The apparent dihedral angles around θ were more likely to be observed on the polished section than the other angles. The median of the Y values closely corresponds to θ (Jurewicz & Jurewicz, 1986). We note that a Y smaller than θ requires a smaller ϕ, and vice versa. Increasing sin2Q (i.e., Q) tends to cause Y values to deviate from the median (i.e., θ).

The angle between the grain boundary plane and the arbitrary sectioning plane, F (F = 0–90°) can be calculated from their normals. F is dependent on Q and f, but independent of θ (Figure S1). In Figure S2b, the contours of F are shown in the sin2Q versus f diagram. As in the case of Y, the area fraction of the angles ≥ F should correspond to the probability that the angles become more than or equal to F. At sin2Q (i.e., Q) = 0 or ϕ = 0, the grain boundary plane is vertical (F = 90°). With increasing Q and ϕ, F tends to deviate from 90°: the grain boundary plane becomes more tilted. Therefore, subvertical (i.e., F close to 90°) grain boundary planes can be expected at the triple junction with Y smaller than the median, because such Y values can only be observed at low ϕ.

Combining the Y and F contours in the sin2Q versus ϕ diagram allows us to compute the probability of observing subvertical grain boundary planes at the triple junctions in an arbitrary Y

window on the polished section. We regarded the minimum deviation of F from 90°, which satisfies probability of more than ~68%, as the representative error (1s) of our GBPD analyses. In figure S2c, the area of F ≥ 67° in our preferred Y window from 0° to 65° (i.e., median + 5°) is shown in the sin2Q versus f diagram for θ = 60°. 71% of the apparent dihedral angles fell within the range of 0° ≤ Y ≤ 65° in which 68% of grain boundary planes formed an angle greater than or equal to 67° with respect to the sectioning plane. Thus, we inferred the representative errors of ~23° in our GBPD analyses. Although this value slightly increased and decreased at lower and higher θ, respectively, it was not significantly dependent on θ in the range of interest (23–24° at θ = 50–80°). If we do not use dihedral angle constraints (i.e., Y window of 0–180°), the probability of F ≥ 67° decreases to 49% and the estimated error becomes 35°.

2. Figures S1 to S10. The Supporting Information Figures

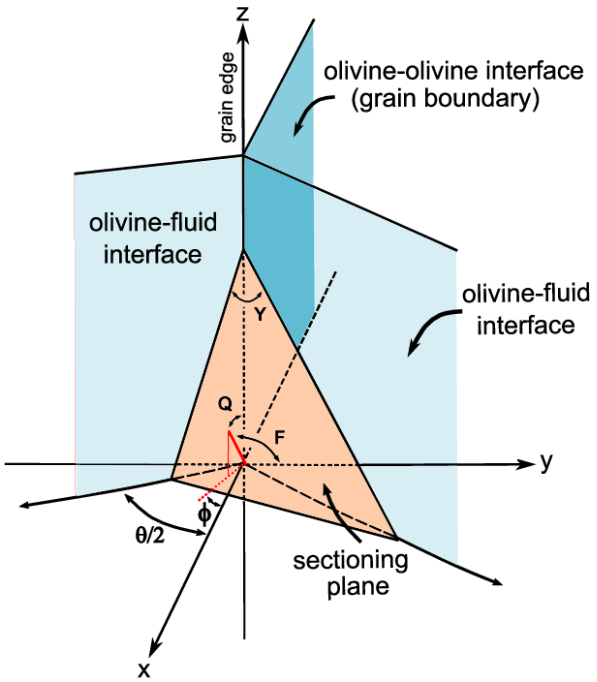

Figure S1. Schematic olivine–olivine–fluid triple junction with a sectioning plane after Jurewicz and Jurewicz (1986). θ is the true dihedral angle formed by two olivine–fluid interfaces (pale blue planes). Y is the apparent dihedral angle observed on the sectioning plane (pale orange plane). The bold red line represents the unit normal of the sectioning plane defined in the angular coordinates Q and ϕ. F is the angle formed by the sectioning plane and grain boundary plane (deep sky–blue plane).

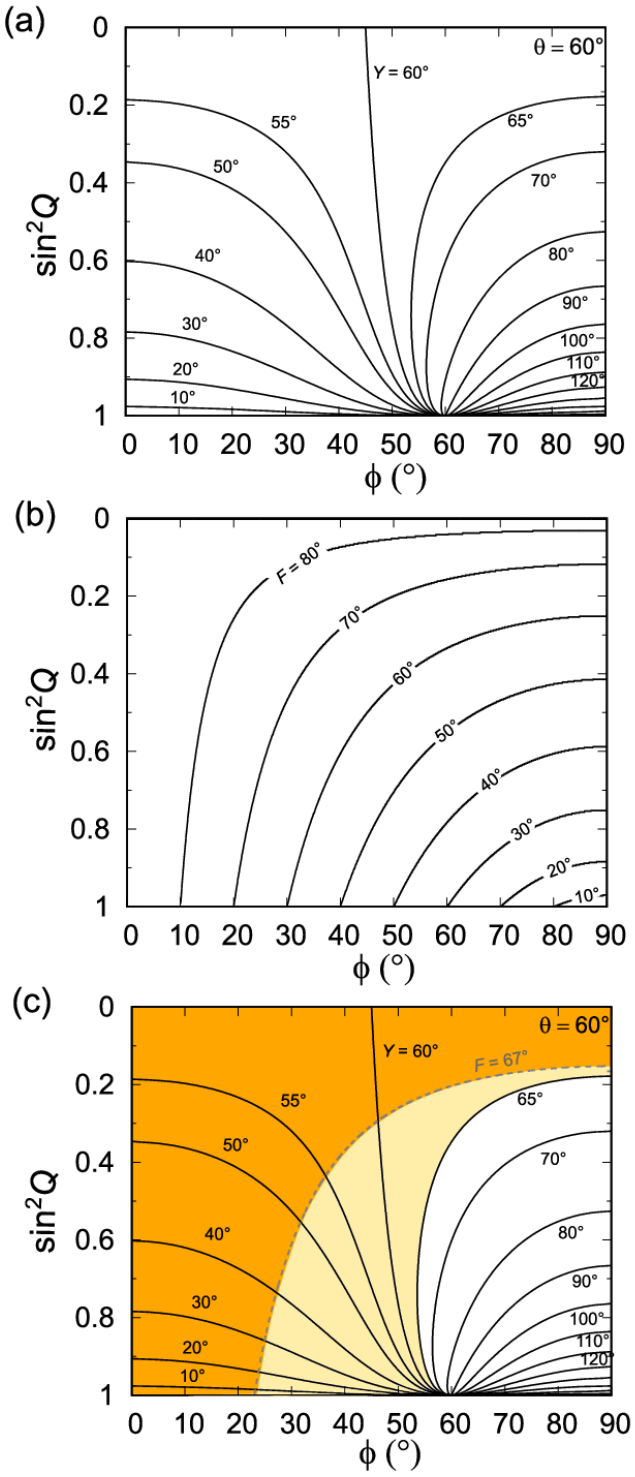

Figure S2. Results of sectioning calculation at the olivine–olivine–fluid triple junction. a, Contours of the apparent dihedral angle, Y in the sin2Q versus ϕ diagram calculated according to Harker and Parker (1945) assuming the true dihedral angle, θ of 60°. **b,** Contours of the angle formed by grain boundary plane and sectioning plane, F in the sin2Q versus ϕ diagram. **c,** The area of F ≥ 67° within the Y window of 0–65° in the sin2Q versus ϕ diagram (orange). The ratio of this area to the area of Y = 0–60° (orange + pale yellow) yields the probability of F ≥ 67° in the selected Y window.

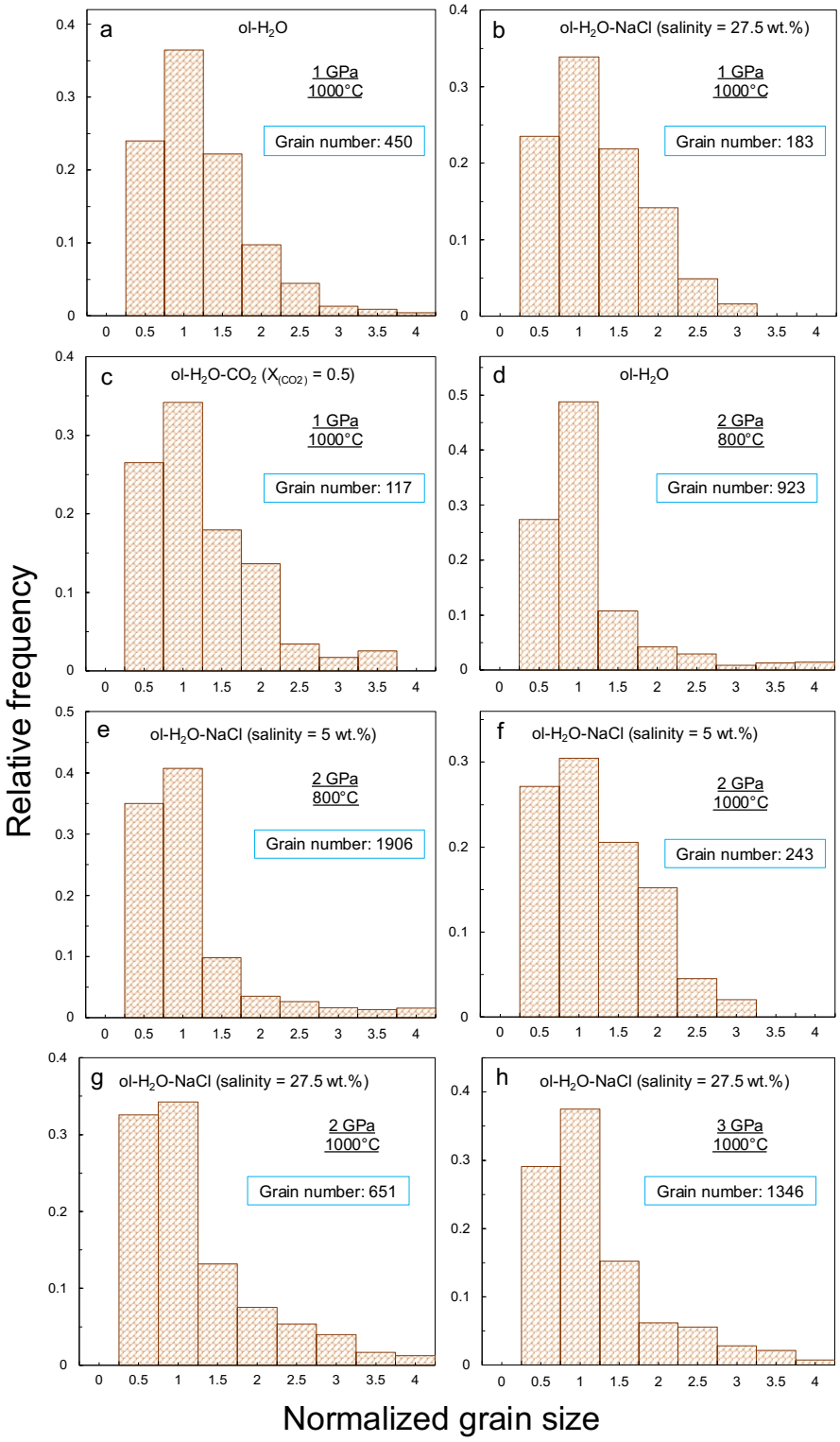

Figure S3. Histogram of the grain size distribution in the olivine–fluid system. The grain size distribution was normalized by the mean grain size of the recovered sample. The grain size is concentrated with a peak around the mean grain size. Abbreviation: ol = olivine.

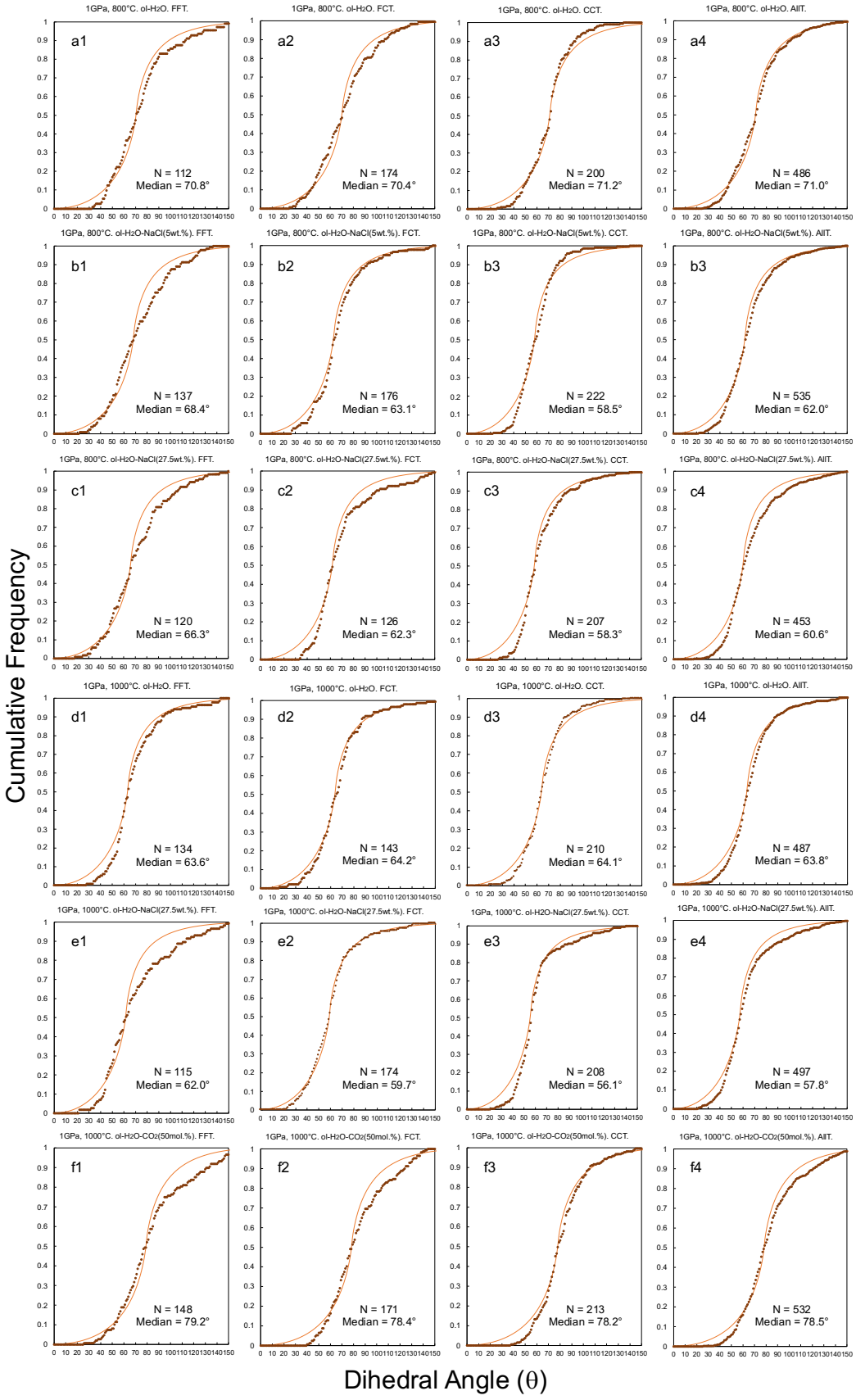
1GPa, 800°C. ol-H2O. FFT.
a1
N = 112
Median = 70.8°
1GPa, 800°C. ol-H2O. FCT.
a2
N = 174
Median = 70.4°
1GPa, 800°C. ol-H2O. CCT.
a3
N = 200
Median = 71.2°
1GPa, 800°C. ol-H2O. AIIT.
a4
N = 486
Median = 71.0°
1GPa, 800°C. ol-H2O-NaCl(5wt.%). FFT.
b1
N = 137
Median = 68.4°
1GPa, 800°C. ol-H2O-NaCl(5wt.%). FCT.
b2
N = 176
Median = 63.1°
1GPa, 800°C. ol-H2O-NaCl(5wt.%). CCT.
b3
N = 222
Median = 58.5°
1GPa, 800°C. ol-H2O-NaCl(5wt.%). AIIT.
b3
N = 535
Median = 62.0°
1GPa, 800°C. ol-H2O-NaCl(27.5wt.%). FFT.
c1
N = 120
Median = 66.3°
1GPa, 800°C. ol-H2O-NaCl(27.5wt.%). FCT.
c2
N = 126
Median = 62.3°
1GPa, 800°C. ol-H2O-NaCl(27.5wt.%). CCT.
c3
N = 207
Median = 58.3°
1GPa, 800°C. ol-H2O-NaCl(27.5wt.%). AIIT.
c4
N = 453
Median = 60.6°
1GPa, 1000°C. ol-H2O. FFT.
d1
N = 134
Median = 63.6°
1GPa, 1000°C. ol-H2O. FCT.
d2
N = 143
Median = 64.2°
1GPa, 1000°C. ol-H2O. CCT.
d3
N = 210
Median = 64.1°
1GPa, 1000°C. ol-H2O. AIIT.
d4
N = 487
Median = 63.8°
1GPa, 1000°C. ol-H2O-NaCl(27.5wt.%). FFT.
e1
N = 115
Median = 62.0°
1GPa, 1000°C. ol-H2O-NaCl(27.5wt.%). FCT.
e2
N = 174
Median = 59.7°
1GPa, 1000°C. ol-H2O-NaCl(27.5wt.%). CCT.
e3
N = 208
Median = 56.1°
1GPa, 1000°C. ol-H2O-NaCl(27.5wt.%). AIIT.
e4
N = 497
Median = 57.8°
1GPa, 1000°C. ol-H2O-CO2(50mol.%). FFT.
f1
N = 148
Median = 79.2°
1GPa, 1000°C. ol-H2O-CO2(50mol.%). FCT.
f2
N = 171
Median = 78.4°
1GPa, 1000°C. ol-H2O-CO2(50mol.%). CCT.
f3
N = 213
Median = 78.2°
1GPa, 1000°C. ol-H2O-CO2(50mol.%). AIIT.
f4
N = 532
Median = 78.5°
Cumulative Frequency
Dihedral Angle (θ)

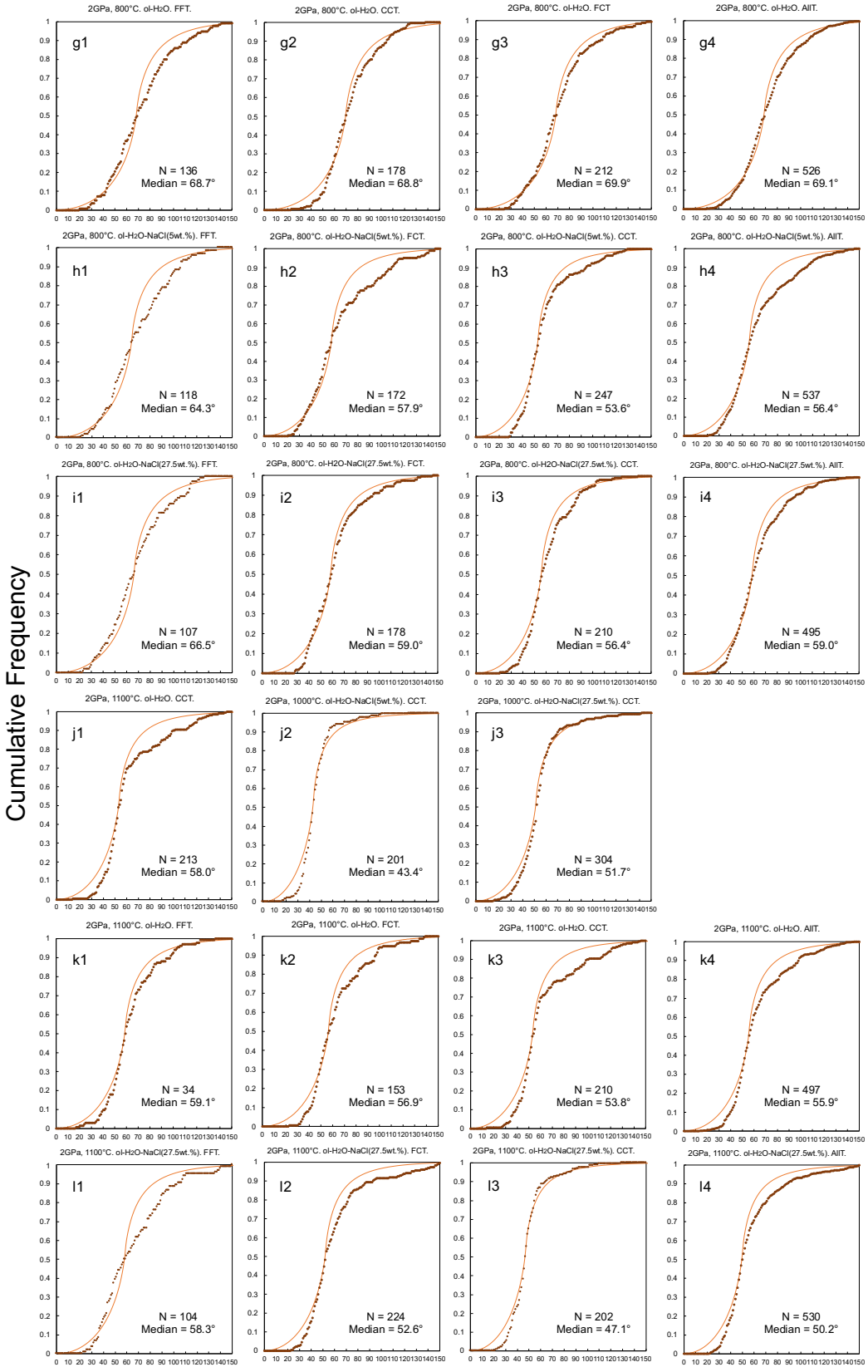
2GPa, 800°C. ol-H2O. FFT.
g1
N = 136
Median = 68.7°
2GPa, 800°C. ol-H2O. CCT.
g2
N = 178
Median = 68.8°
2GPa, 800°C. ol-H2O. FCT
g3
N = 212
Median = 69.9°
2GPa, 800°C. ol-H2O. AllT.
g4
N = 526
Median = 69.1°
2GPa, 800°C. ol-H2O-NaCl(5wt.%). FFT.
h1
N = 118
Median = 64.3°
2GPa, 800°C. ol-H2O-NaCl(5wt.%). FCT.
h2
N = 172
Median = 57.9°
2GPa, 800°C. ol-H2O-NaCl(5wt.%). CCT.
h3
N = 247
Median = 53.6°
2GPa, 800°C. ol-H2O-NaCl(5wt.%). AllT.
h4
N = 537
Median = 56.4°
2GPa, 800°C. ol-H2O-NaCl(27.5wt.%). FFT.
i1
N = 107
Median = 66.5°
2GPa, 800°C. ol-H2O-NaCl(27.5wt.%). FCT.
i2
N = 178
Median = 59.0°
2GPa, 800°C. ol-H2O-NaCl(27.5wt.%). CCT.
i3
N = 210
Median = 56.4°
2GPa, 800°C. ol-H2O-NaCl(27.5wt.%). AllT.
i4
N = 495
Median = 59.0°
2GPa, 1100°C. ol-H2O. CCT.
j1
N = 213
Median = 58.0°
2GPa, 1000°C. ol-H2O-NaCl(5wt.%). CCT.
j2
N = 201
Median = 43.4°
2GPa, 1000°C. ol-H2O-NaCl(27.5wt.%). CCT.
j3
N = 304
Median = 51.7°
2GPa, 1100°C. ol-H2O. FFT.
k1
N = 34
Median = 59.1°
2GPa, 1100°C. ol-H2O. FCT.
k2
N = 153
Median = 56.9°
2GPa, 1100°C. ol-H2O. CCT.
k3
N = 210
Median = 53.8°
2GPa, 1100°C. ol-H2O. AllT.
k4
N = 497
Median = 55.9°
2GPa, 1100°C. ol-H2O-NaCl(27.5wt.%). FFT.
l1
N = 104
Median = 58.3°
2GPa, 1100°C. ol-H2O-NaCl(27.5wt.%). FCT.
l2
N = 224
Median = 52.6°
2GPa, 1100°C. ol-H2O-NaCl(27.5wt.%). CCT.
l3
N = 202
Median = 47.1°
2GPa, 1100°C. ol-H2O-NaCl(27.5wt.%). AllT.
l4
N = 530
Median = 50.2°
Cumulative Frequency
Dihedral Angle (θ)

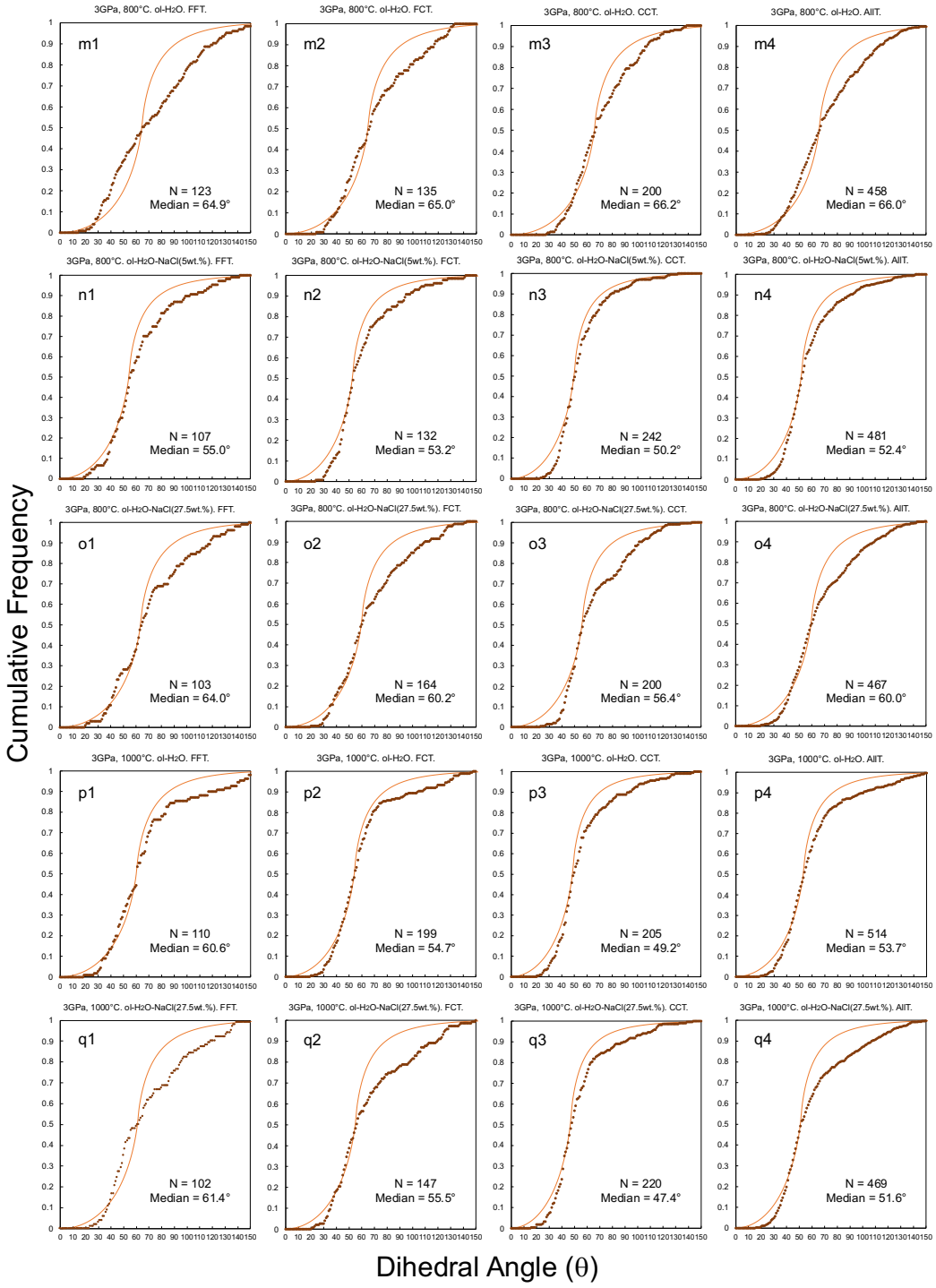

Figure S4. Cumulative frequency curves of measured apparent dihedral angles (θ) in olivine–fluid systems at 1–3 GPa and 800–1100 °C. The median value and number (N) of the measured angles are shown for each experimental condition. The solid lines represent the theoretical cumulative frequency curves of the isotropic system with one true θ (Jurewicz & Jurewicz, 1986). This angle is assumed to coincide with the obtained median value. The P–T and fluid composition are shown for each system. Abbreviations: ol=olivine, FFT = faceted–faceted type angle, FCT = faceted–curved type angle, CCT= curved–curved type angle, AllT= all type of measured angle.

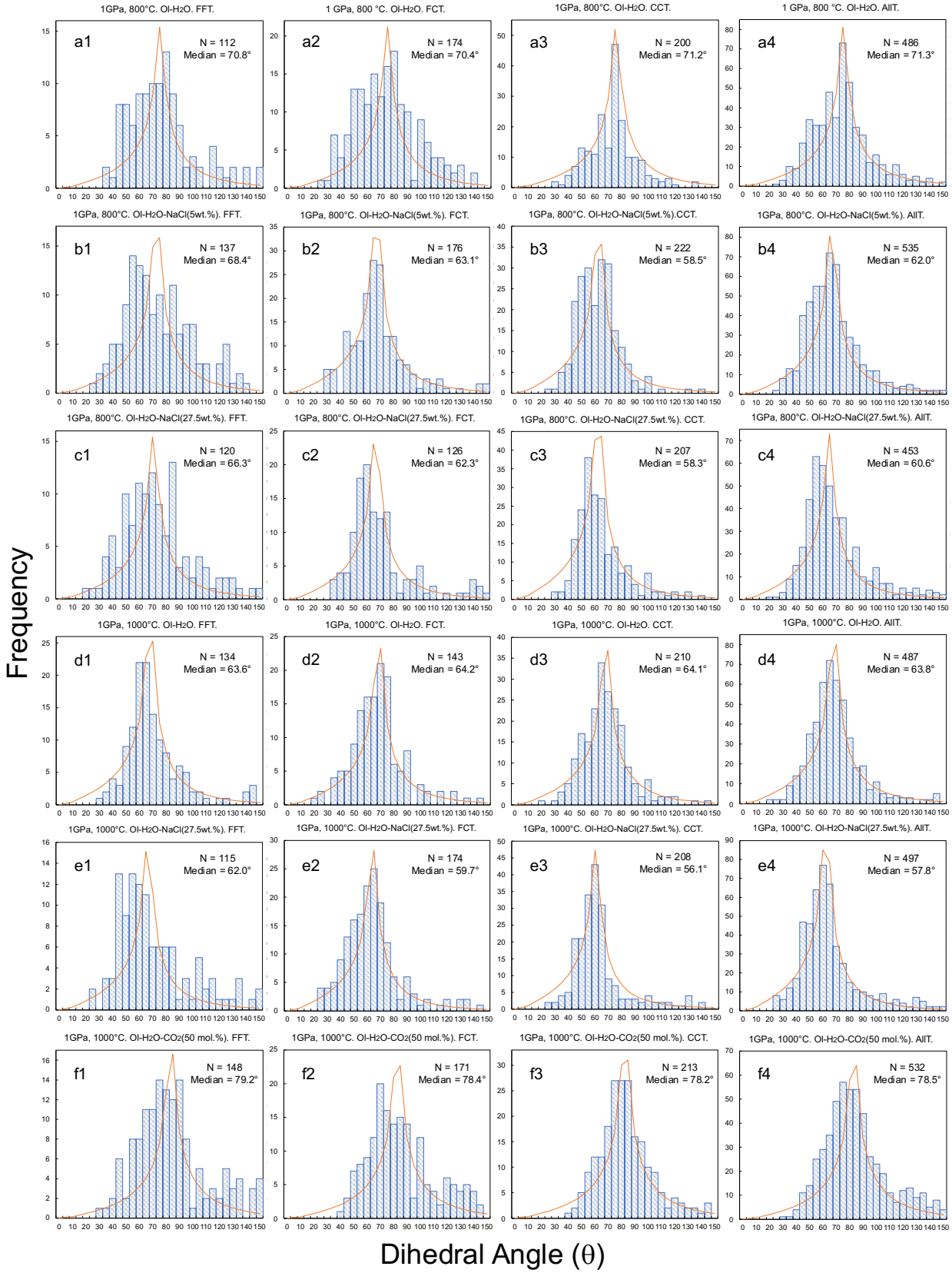
1GPa, 800°C. Ol-H2O. FFT.
a1
N = 112
Median = 70.8°
1 GPa, 800 °C. Ol-H2O. FCT.
a2
N = 174
Median = 70.4°
1GPa, 800°C. Ol-H2O. CCT.
a3
N = 200
Median = 71.2°
1 GPa, 800 °C. Ol-H2O. AllT.
a4
N = 486
Median = 71.3°
1GPa, 800°C. Ol-H2O-NaCl(5wt.%). FFT.
b1
N = 137
Median = 68.4°
1GPa, 800°C. Ol-H2O-NaCl(5wt.%). FCT.
b2
N = 176
Median = 63.1°
1GPa, 800°C. Ol-H2O-NaCl(5wt.%).CCT.
b3
N = 222
Median = 58.5°
1GPa, 800°C. Ol-H2O-NaCl(5wt.%). AllT.
b4
N = 535
Median = 62.0°
1GPa, 800°C. Ol-H2O-NaCl(27.5wt.%). FFT.
c1
N = 120
Median = 66.3°
1GPa, 800°C. Ol-H2O-NaCl(27.5wt.%). FCT.
c2
N = 126
Median = 62.3°
1GPa, 800°C. Ol-H2O-NaCl(27.5wt.%). CCT.
c3
N = 207
Median = 58.3°
1GPa, 800°C. Ol-H2O-NaCl(27.5wt.%). AllT.
c4
N = 453
Median = 60.6°
1GPa, 1000°C. Ol-H2O. FFT.
d1
N = 134
Median = 63.6°
1GPa, 1000°C. Ol-H2O. FCT.
d2
N = 143
Median = 64.2°
1GPa, 1000°C. Ol-H2O. CCT.
d3
N = 210
Median = 64.1°
1GPa, 1000°C. Ol-H2O. AllT.
d4
N = 487
Median = 63.8°
1GPa, 1000°C. Ol-H2O-NaCl(27.5wt.%). FFT.
e1
N = 115
Median = 62.0°
1GPa, 1000°C. Ol-H2O-NaCl(27.5wt.%). FCT.
e2
N = 174
Median = 59.7°
1GPa, 1000°C. Ol-H2O-NaCl(27.5wt.%). CCT.
e3
N = 208
Median = 56.1°
1GPa, 1000°C. Ol-H2O-NaCl(27.5wt.%). AllT.
e4
N = 497
Median = 57.8°
1GPa, 1000°C. Ol-H2O-CO2(50 mol.%). FFT.
f1
N = 148
Median = 79.2°
1GPa, 1000°C. Ol-H2O-CO2(50 mol.%). FCT.
f2
N = 171
Median = 78.4°
1GPa, 1000°C. Ol-H2O-CO2(50 mol.%). CCT.
f3
N = 213
Median = 78.2°
1GPa, 1000°C. Ol-H2O-CO2(50 mol.%). AllT.
f4
N = 532
Median = 78.5°
Frequency
Dihedral Angle (θ)

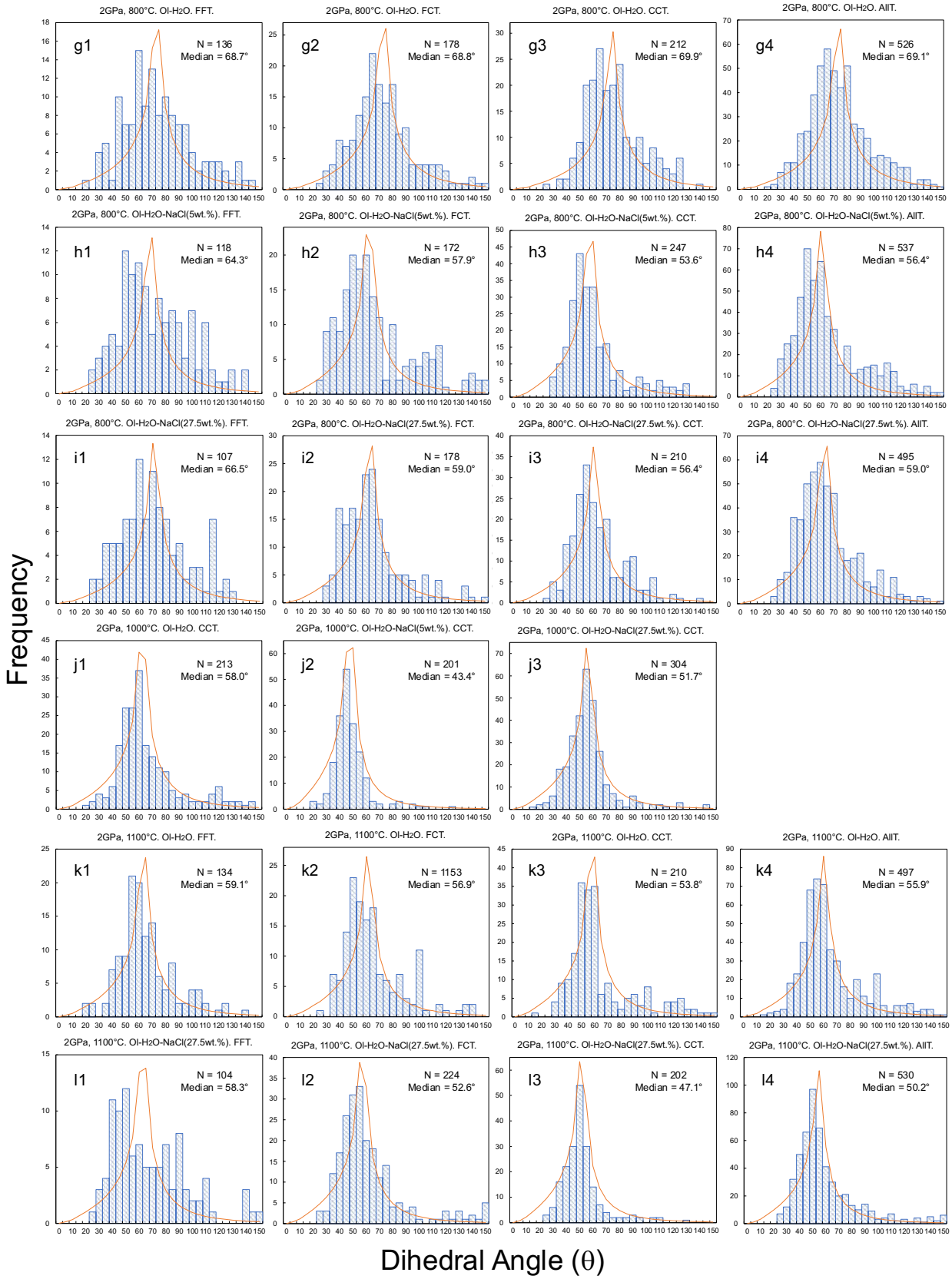
2GPa, 800°C. Ol-H2O. FFT.
g1
N = 136
Median = 68.7°
2GPa, 800°C. Ol-H2O. FCT.
g2
N = 178
Median = 68.8°
2GPa, 800°C. Ol-H2O. CCT.
g3
N = 212
Median = 69.9°
2GPa, 800°C. Ol-H2O. AllT.
g4
N = 526
Median = 69.1°
2GPa, 800°C. Ol-H2O-NaCl(5wt.%). FFT.
h1
N = 118
Median = 64.3°
2GPa, 800°C. Ol-H2O-NaCl(5wt.%). FCT.
h2
N = 172
Median = 57.9°
2GPa, 800°C. Ol-H2O-NaCl(5wt.%). CCT.
h3
N = 247
Median = 53.6°
2GPa, 800°C. Ol-H2O-NaCl(5wt.%). AllT.
h4
N = 537
Median = 56.4°
2GPa, 800°C. Ol-H2O-NaCl(27.5wt.%). FFT.
i1
N = 107
Median = 66.5°
2GPa, 800°C. Ol-H2O-NaCl(27.5wt.%). FCT.
i2
N = 178
Median = 59.0°
2GPa, 800°C. Ol-H2O-NaCl(27.5wt.%). CCT.
i3
N = 210
Median = 56.4°
2GPa, 800°C. Ol-H2O-NaCl(27.5wt.%). AllT.
i4
N = 495
Median = 59.0°
2GPa, 1000°C. Ol-H2O. CCT.
j1
N = 213
Median = 58.0°
2GPa, 1000°C. Ol-H2O-NaCl(5wt.%). CCT.
j2
N = 201
Median = 43.4°
2GPa, 1000°C. Ol-H2O-NaCl(27.5wt.%). CCT.
j3
N = 304
Median = 51.7°
2GPa, 1100°C. Ol-H2O. FFT.
k1
N = 134
Median = 59.1°
2GPa, 1100°C. Ol-H2O. FCT.
k2
N = 1153
Median = 56.9°
2GPa, 1100°C. Ol-H2O. CCT.
k3
N = 210
Median = 53.8°
2GPa, 1100°C. Ol-H2O. AllT.
k4
N = 497
Median = 55.9°
2GPa, 1100°C. Ol-H2O-NaCl(27.5wt.%). FFT.
l1
N = 104
Median = 58.3°
2GPa, 1100°C. Ol-H2O-NaCl(27.5wt.%). FCT.
l2
N = 224
Median = 52.6°
2GPa, 1100°C. Ol-H2O-NaCl(27.5wt.%). CCT.
l3
N = 202
Median = 47.1°
2GPa, 1100°C. Ol-H2O-NaCl(27.5wt.%). AllT.
l4
N = 530
Median = 50.2°
Frequency
Dihedral Angle (θ)

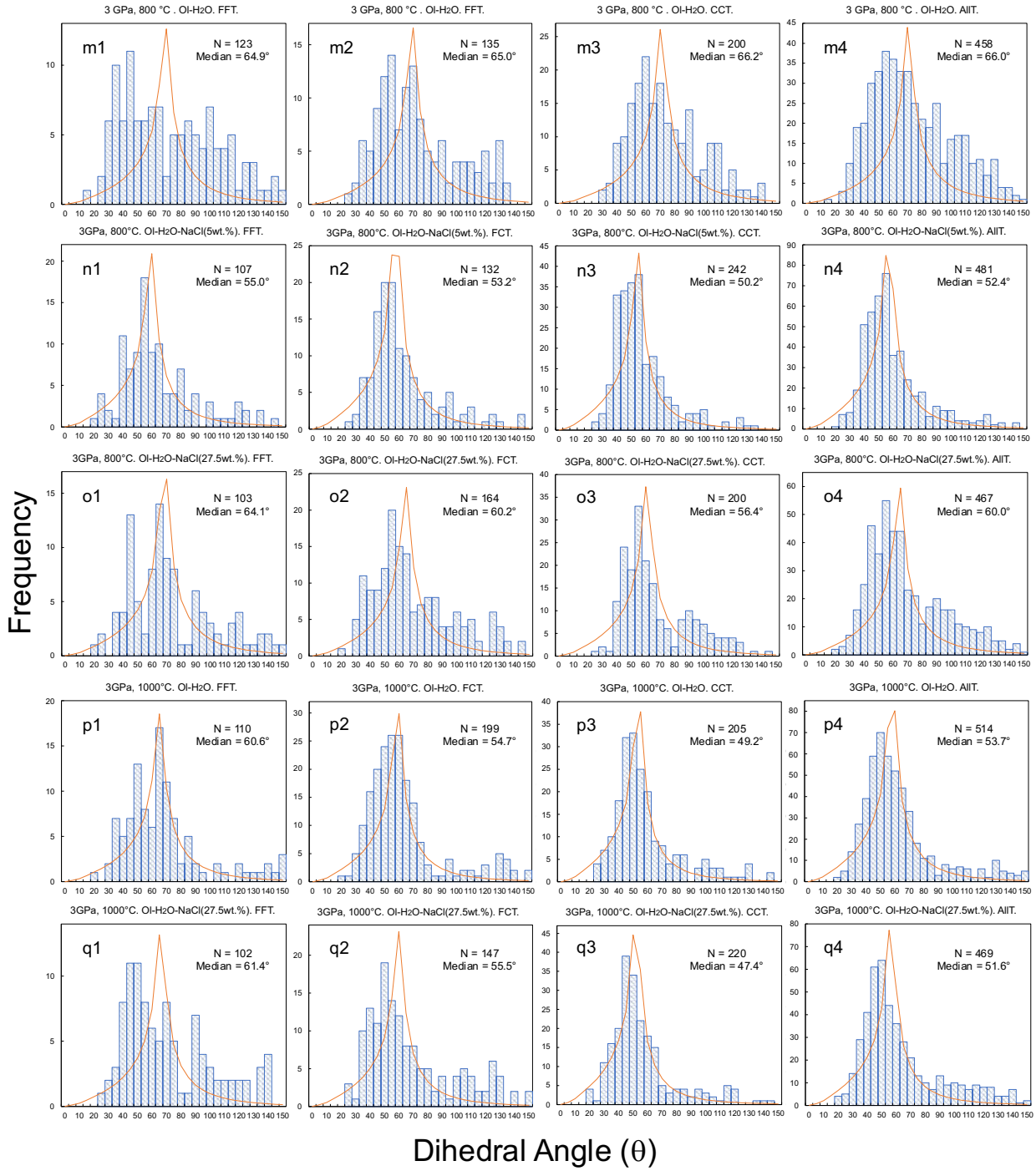

Figure S5. Frequency distribution histograms of measured apparent dihedral angles (θ) in olivine–fluid systems at 1–3 GPa and 800–1100 °C. Theoretical distributions (orange curves) for the mono–mineralic and isotropic systems are also shown in the histograms along with the median values (Jurewicz & Jurewicz, 1986). The P–T and fluid composition are shown for each system. Abbreviations: ol=olivine, FFT = faceted–faceted type angle, FCT = faceted–curved type angle, CCT= curved–curved type angle, AllT= all type of measured angle.

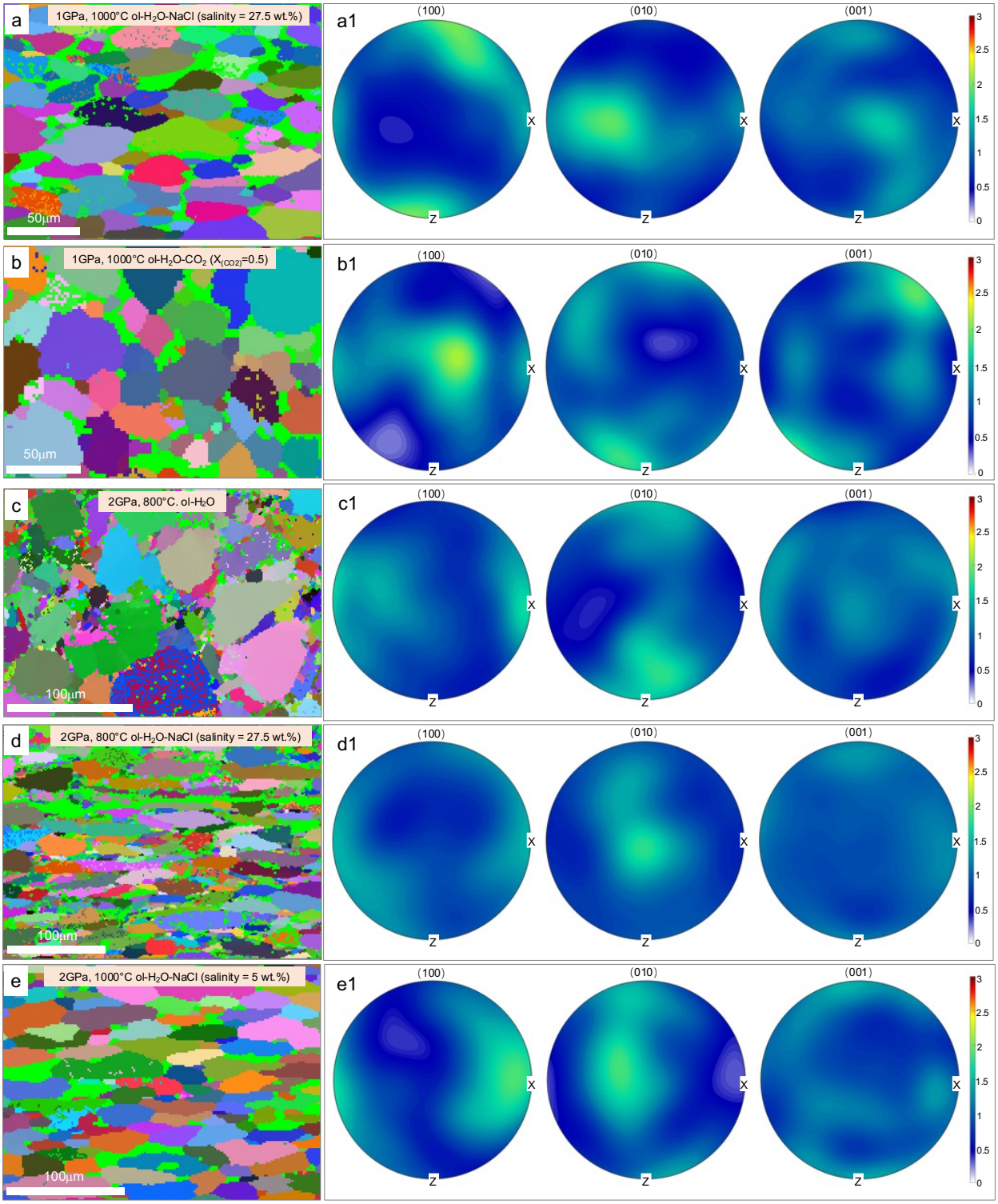

Figure S6. EBSD maps and corresponding Pole figures under static compression conditions. a–e, EBSD maps of recovered olivine aggregate in olivine–fluid systems. The small points within grain are attributed to the noise, crystal defects, and fluid inclusions, which are mostly removed via denoise processes while making pole figure. The crack in c was formed during the decompression, and the mapping direction was calibrated during the EBSD data process. In these systems, all grains are olivine with different orientations. **a1–e1**, Pole figures to show the crystallographic orientation of (100), (010), and (001) corresponding to a–e. The intensities in the color bar are in multiples of the random distribution. The P–T condition and fluid composition are shown along with the corresponding system. Abbreviation: ol=olivine.

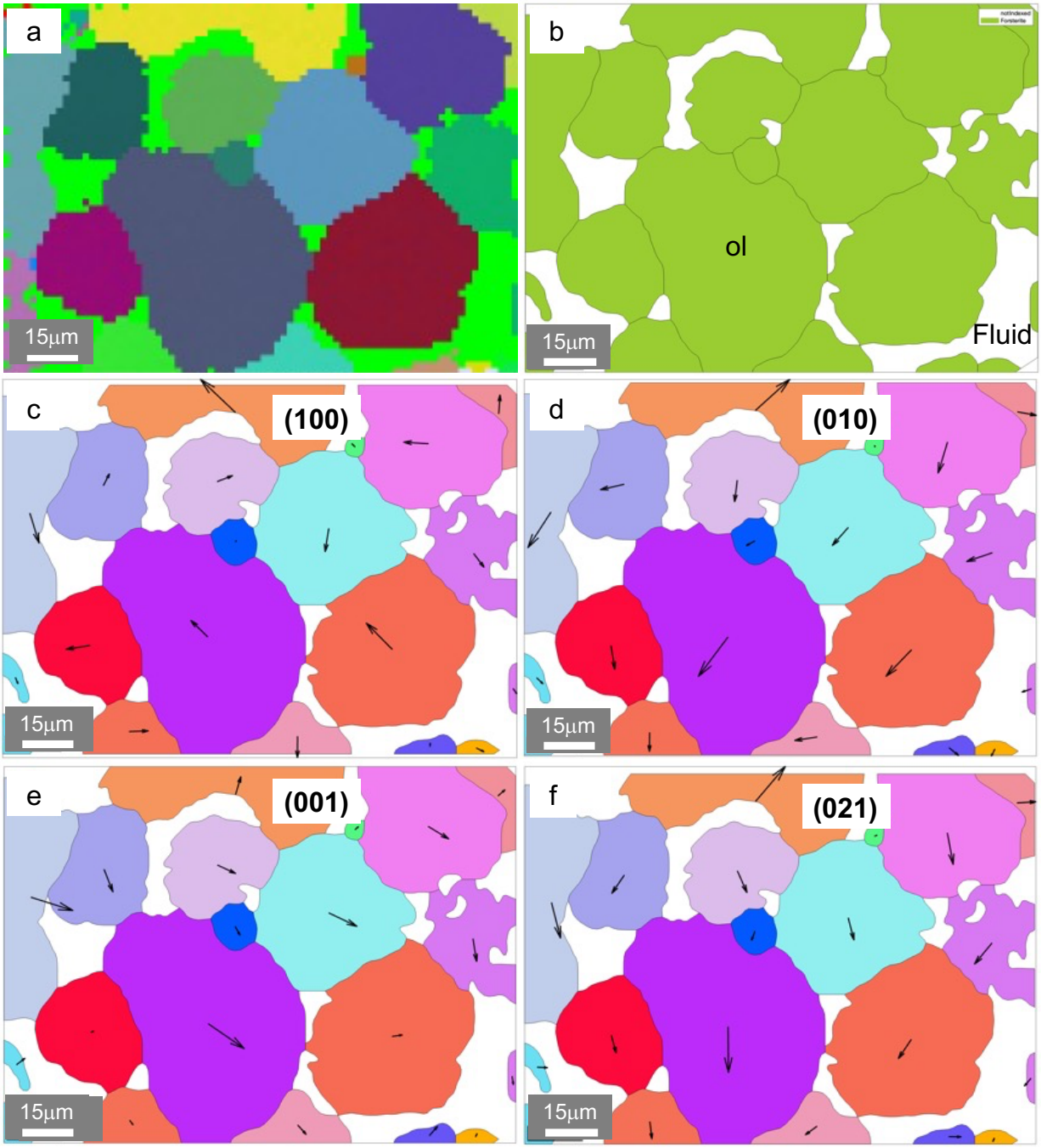

Figure S7. EBSD data and olivine orientation in the H2O system at 1 GPa and 1000°C. a, EBSD map with denoise process. **b**, Grain image reconstruction produced by MTEX toolbox in MATLAB. **c–f**, Special crystal orientation in 2–D grain image given by MTEX toolbox in MATLAB. The orientation is shown for each system. The orientations sometime seem similar or overlapped in 2–D image, it is necessary to check the 3–D spatial orientation while compilation. All grains in figure are olivine.

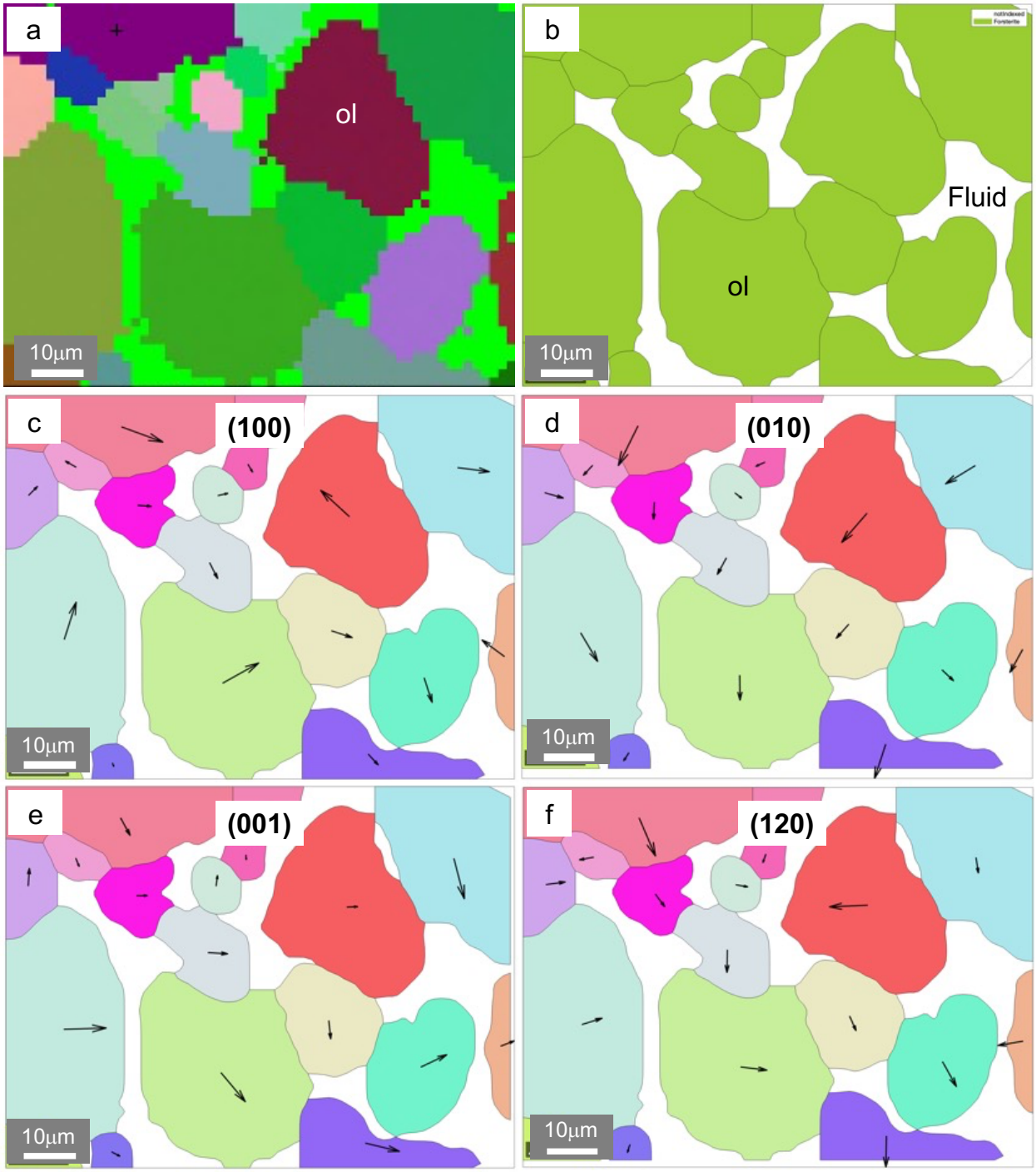

Figure S8. EBSD data and olivine orientation in the H_2O–CO_2($X_{(CO2)}$=0.5) system at 1 GPa and 1000°C. **a**, EBSD map with denoise process. **b**, Grain image reconstruction produced by MTEX toolbox in MATLAB. **c–f**, Special crystal orientation in 2–D grain image given by MTEX toolbox in MATLAB. The orientation is shown for each system. The orientations sometime seem similar or overlapped in 2–D image, it is necessary to check the 3–D spatial orientation while compilation. All grains in figure are olivine.

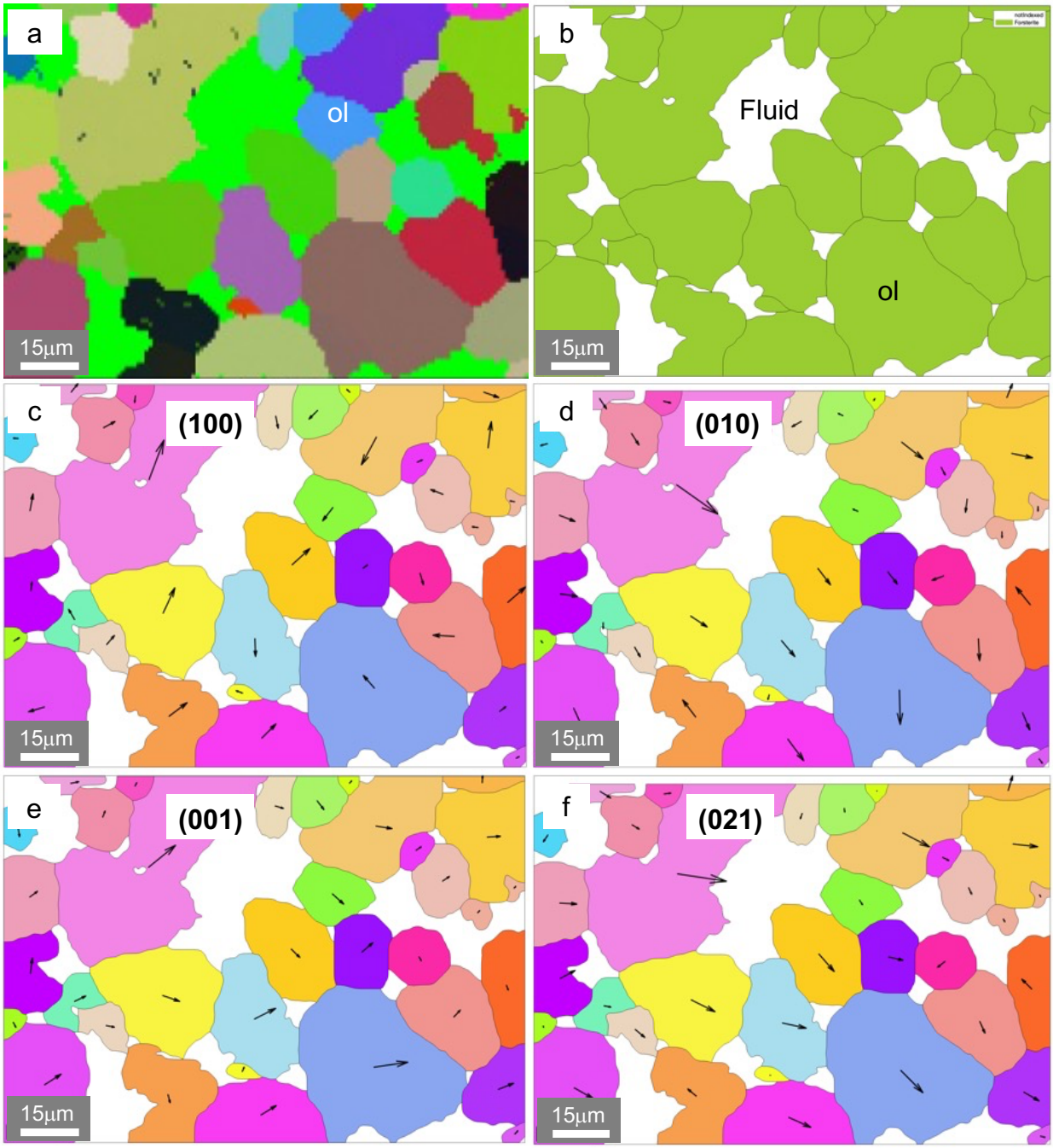

Figure S9. EBSD data and olivine orientation in the H_2O system at 2 GPa and 1000°C. a, EBSD map with denoise process. **b**, Grain image reconstruction produced by MTEX toolbox in MATLAB. **c–f**, Special crystal orientation in 2–D grain image given by MTEX toolbox in MATLAB. The orientation is shown for each system. The orientations sometime seem similar or overlapped in 2–D image, it is necessary to check the 3–D spatial orientation while compilation. All grains in figure are olivine.

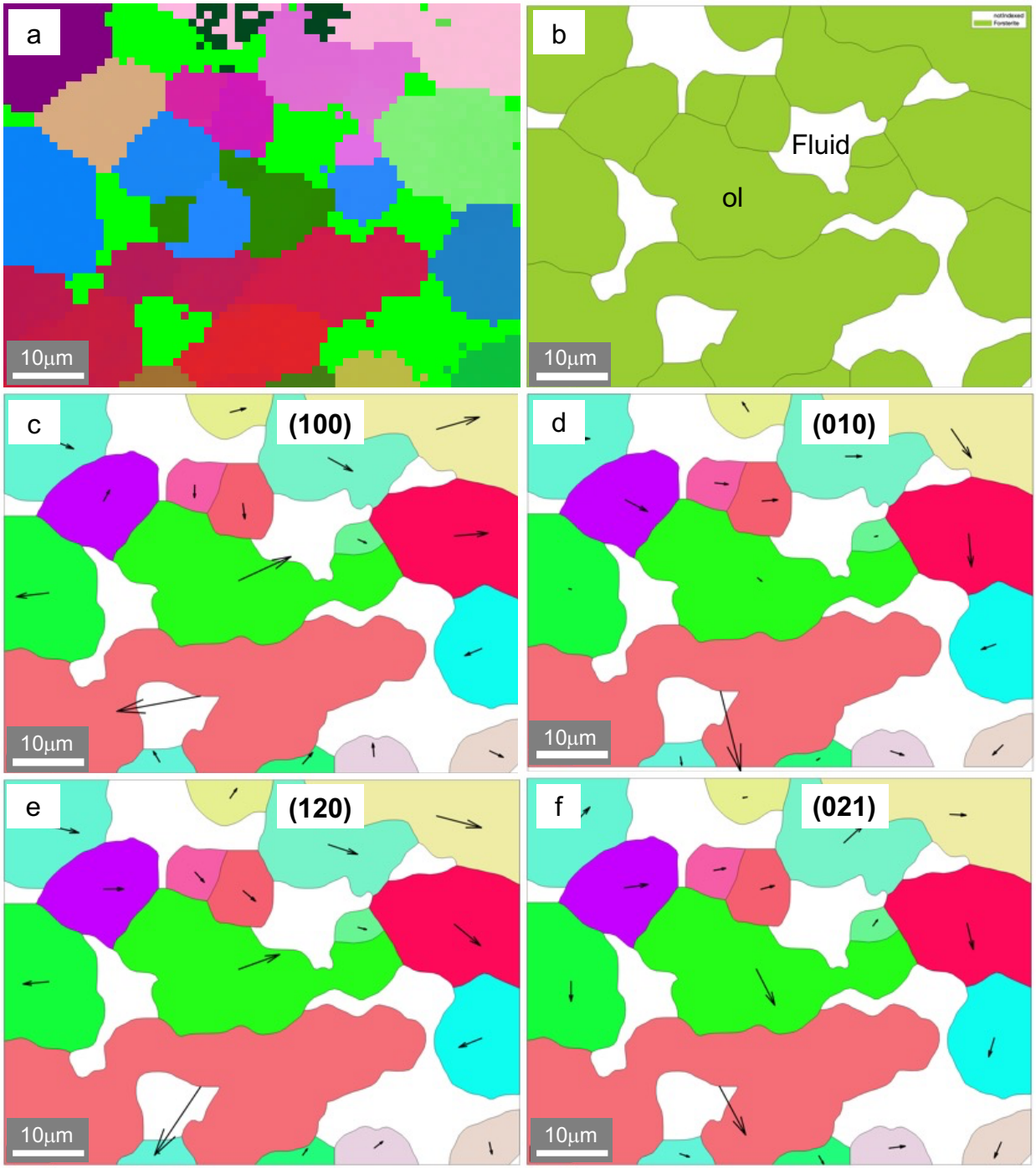

Figure S10. EBSD data and olivine orentation in the H_2O–NaCl (27.5wt%) system at 2 GPa and 1000°C. **a**, EBSD map with denoise process. **b**, Grain image reconstruction produced by MTEX toolbox in MATLAB. **c–f**, Special crystal orientation in 2–D grain image given by MTEX toolbox in MATLAB. The orientation is shown for each system. The orientations sometime seem similar or overlapped in 2–D image, it is necessary to check the 3–D spatial orientation while compilation. All grains in figure are olivine.

3. Table 1. List of calculated FF–type dihedral angles formed by low–Miller Index grain boundary planes and interfaces with fluid at a triple junction

Grain Boundary Plane	Faceted Interface	C1 \ C2	*25.0*	*43.0*	*38.5*	*47.0*	*40.7*	*66.2*	*55.1*	*51.5*	*44.8*	Flat face
100	110	*25.0*	**50.0***	68.0	63.5	72.0	65.7	91.2	80.1	76.5	69.8	25.0
100	120	*43.0*	68.0*	**86.0**	81.5	90.0	83.7	109.2	98.1	94.5	87.8	43.0
100	101	*38.5*	63.5*	81.5*	**77.0***	85.5	79.2	104.7	93.6	90.0	83.3	38.5
010	120	*47.0*	72.0	90.0	85.5	**94.0**	87.7	113.2	102.1	98.5	91.8	47.0
010	021	*40.7*	65.7*	83.7	79.2*	87.7	**81.4***	106.9	95.8	92.2	85.5	40.7
101	021	*66.2*	91.2	109.2	104.7	113.2	106.9	**132.4**	121.3	117.7	111	66.2*
101	120	*55.1*	80.1*	98.1	93.6	102.1	95.8	121.3	**110.2**	106.6	99.9	55.1*
101	001	*51.5*	76.5*	94.5	90.0	98.5	92.2	117.7	106.6	**103**	96.3	51.5*
101	110	*44.8*	69.8*	87.8	83.3	91.8	85.5	111.0	99.9	96.3	**89.6**	44.8

Bold represents symmetric configuration.

The star superscript represents calculated angles that are consistent with experimental data.